Received: 20 January 2022 | Revised: 22 April 2022 | Accepted: 19 May 2022

DOI: 10.1002/inf2.12341

REVIEW

WILEY

Two-dimensional In_2Se_3: A rising advanced material for ferroelectric data storage

Yu-Ting Huang[1] | Nian-Ke Chen[1] | Zhen-Ze Li[1] | Xue-Peng Wang[1] | Hong-Bo Sun[1,2] | Shengbai Zhang[3] | Xian-Bin Li[1]

[1]State Key Laboratory of Integrated Optoelectronics, College of Electronic Science and Engineering, Jilin University, Changchun, China

[2]State Key Lab of Precision Measurement Technology and Instruments, Department of Precision Instrument, Tsinghua University, Beijing, China

[3]Department of Physics, Applied Physics, and Astronomy, Rensselaer Polytechnic Institute, Troy, New York, USA

Correspondence
Xian-Bin Li, State Key Laboratory of Integrated Optoelectronics, College of Electronic Science and Engineering, Jilin University, Changchun 130012, China.
Email: lixianbin@jlu.edu.cn

Funding information
China Postdoctoral Science Foundation, Grant/Award Number: 2019M661200; National Natural Science Foundation of China, Grant/Award Numbers: 11874171, 11904118, 61922035; Fundamental Research Funds for the Central Universities

Abstract

Ferroelectric memory is a promising candidate for next-generation nonvolatile memory owing to its outstanding performance such as low power consumption, fast speed, and high endurance. However, the ferroelectricity of conventional ferroelectric materials will be eliminated by the depolarization field when the size drops to the nanometer scale. As a result, the miniaturization of ferroelectric devices was hindered, which makes ferroelectric memory unable to keep up with the development of integrated-circuit (IC) miniaturization. Recently, a two-dimensional (2D) In_2Se_3 was reported to maintain stable ferroelectricity at the ultrathin scale, which is expected to break through the bottleneck of miniaturization. Soon, devices based on 2D In_2Se_3, including the ferroelectric field-effect transistor, ferroelectric channel transistor, synaptic ferroelectric semiconductor junction, and ferroelectric memristor were demonstrated. However, a comprehensive understanding of the structures and the ferroelectric-switching mechanism of 2D In_2Se_3 is still lacking. Here, the atomic structures of different phases, the dynamic mechanism of ferroelectric switching, and the performance/functions of the latest devices of 2D In_2Se_3 are reviewed. Furthermore, the correlations among the structures, the properties, and the device performance are analyzed. Finally, several crucial problems or challenges and possible research directions are put forward. We hope that this review paper can provide timely knowledge and help for the research community to develop 2D In_2Se_3 based ferroelectric memory and computing technology for practical industrial applications.

KEYWORDS

2D ferroelectric device, 2D ferroelectric material, 2D In_2Se_3, neuromorphic computing, nonvolatile memory

Yu-Ting Huang and Nian-Ke Chen contributed equally to this work.

1 | INTRODUCTION

With the rapid development of electronic technology, smart phones, digital cameras, and laptops have become an indispensable part of life. The popularity of these equipments has greatly increased the total amount of data. At the same time, the gradual rise of the Internet of Things, big data, and artificial intelligence industries has also accelerated the growth rate of electronic information.[1–3] The advent of the era of big data means the demand for high-density nonvolatile storage technology, which will undoubtedly trigger a hardware revolution.[4] Therefore, it is urgent for researchers to develop the corresponding devices with high memory density and low power consumption.[5] International Technology Roadmap for Semiconductors (ITRS) has recommended several types of emerging memories, including ferroelectric random access memory (FeRAM), magnetic random access memory (MRAM), phase-change memory (PCM), and resistive random access memory (RRAM).[6] Among them, ferroelectric memory is a potential ideal choice because of its fast operation and intrinsic advantage of low power consumption through electric voltage encoding (rather than the electric current).[7–9]

Ferroelectric memory has a long history since it was first proposed in 1952 by Dudley Allen Buck.[10] The physical basis of ferroelectric memory is based on switchable spontaneous polarization in ferroelectric materials that can be controlled by the external electric field (see Figure 1A).[15] Then, the binary (0/1) electronic information can be

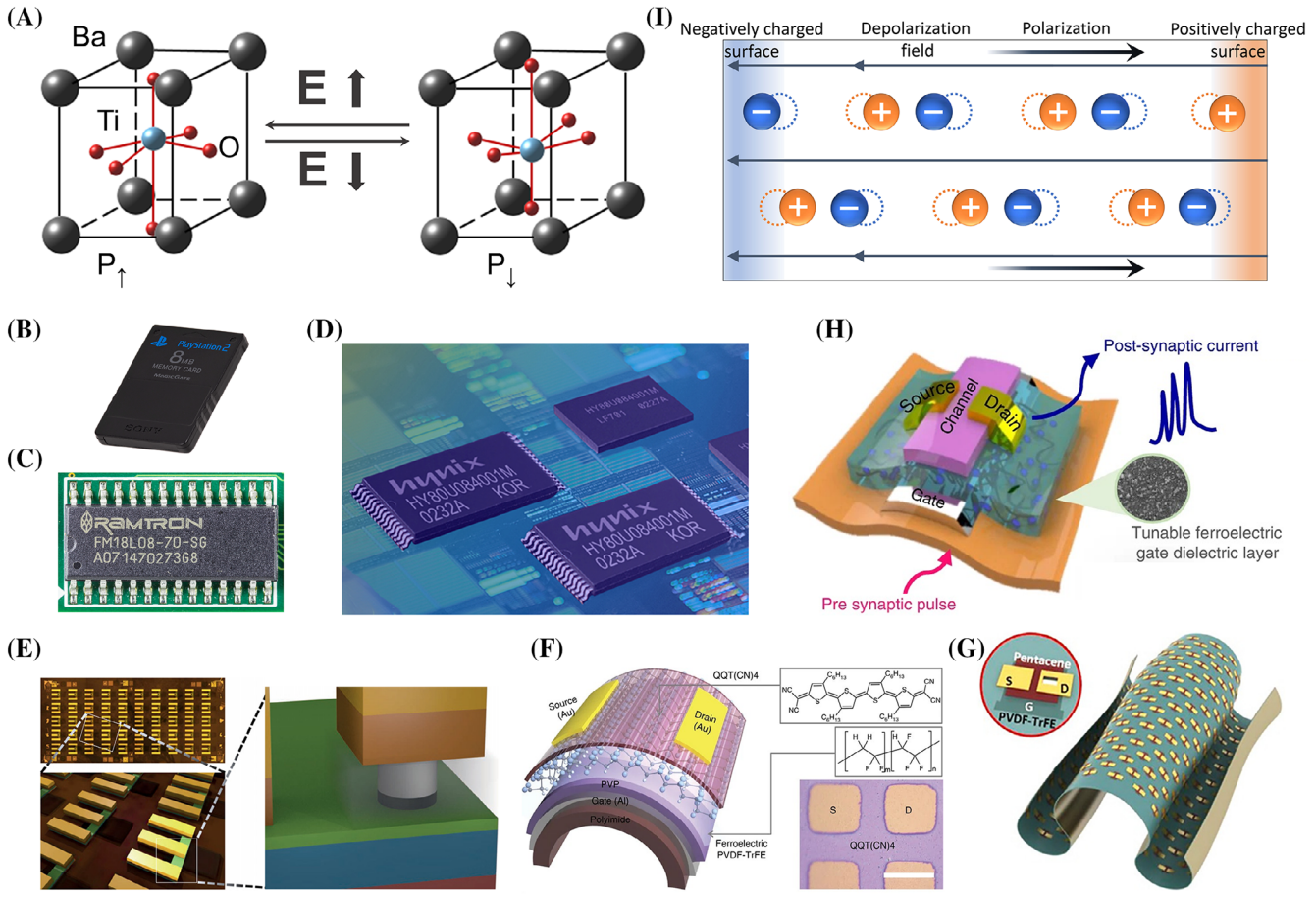

FIGURE 1 (A) Principles of ferroelectric switching, the direction of polarization always tends to be consistent with the external electric field. (B) The ferroelectric memory card of PlayStation 2. (C) 256 K bit nonvolatile ferroelectric random-access memory (FeRAM) developed by the Ramtron company. (D) 4/8 M bit FeRAM introduced by SK Hynix. (E) Optical image (left) and 3D sketch (right) of $BiFeO_3$ ferroelectric tunnel junction. Reproduced with permission.[11] Copyright 2014, AIP Publishing. (F) The schematic of an ultraflexible ferroelectric field-effect transistor (FeFET) memory device, a 300-nm-thick PVDF-TrFE ferroelectric layer is used as the gate insulator. Reproduced with permission.[12] Copyright 2014, Springer Nature. (G) Schematic structure of the flexible FeFET based on 415 nm thick PVDF-TrFE. Reproduced with permission.[13] Copyright 2019, American Chemical Society. (H) Sketch of a flexible FeFET synaptic device, the electrical gate bias voltage act as presynaptic input, and the drain current is regarded as post-synaptic current. Reproduced with permission.[14] Copyright 2020, Springer Nature. (I) The ferroelectric polarization induced by the separation of positively and negatively charge ions, and the depolarization field induced by the positively/negatively charged surfaces

stored in the two polarization states in opposite directions. Such a data recording is rewritable, fast, nonvolatile, and low power consumption.[16–19] It has attracted a lot of attention in the semiconductor industry due to its great potential in practical applications. Several types of devices were developed and partly commercialized. For example, Figure 1B–D shows some representative products based on ferroelectrics, including the memory card used in the well-known PlayStation 2 released by Sony in 2000 (Figure 1B),[20] the 256 K bit nonvolatile FeRAM developed by Ramtron company in 2001 (Figure 1C),[21] and the 4/8 M bit FeRAM with a data access time of 70 ns introduced by SK Hynix in 2003 (Figure 1D).[22] Recently, some new types of ferroelectric memory are invented, such as the ferroelectric tunnel junction memory based on $BiFeO_3$ (Figure 1E),[11] the ultraflexible ferroelectric field-effect transistors (FeFET) memory device with a gate insulator of flexible PVDF-TrFE ferroelectric layer (Figure 1F,G),[12,13] and the flexible synaptic device that can be used for neural computing (Figure 1H).[14]

During the past decades, the miniaturization of the device is a core task to achieve high-density integration for integrated-circuit (IC) applications according to Moore's Law.[23] Novel memory/computing devices based on two-dimensional (2D) materials such as transition metal disulfides (TMD), boron nitride (BN), and graphene, have been successfully fabricated.[24,25] Traditional memories such as PCM have also reached sub-10 nanometers (nm).[26] The miniaturization of ferroelectric memory, however, is tightly blocked by the depolarization-field effect caused by the incomplete screening of the bound charges (see Figure 1I).[27,28] The thinner the film thickness, the stronger the depolarization field.[15,28–30] When the material is being scaled down to nanometers, the spontaneous polarization is gradually eliminated.[31,32] Besides, the influences of interfaces, such as the strain and the screening effects from substrates and electrodes, also become significant.[33–35] Therefore, it becomes an essential task for the industry to search new candidates with abilities of ultra-scaling and robust ferroelectricity.

After decades of efforts, some ultrathin ferroelectric materials have been developed.[9] For example, the thickness of conventional ABO_3 ferroelectric films can be reduced to the nanometer scale by choosing specific electrodes and substrates.[36–38] However, the complicated lattice-matching design and fabrication process limit its practical application. In recent years, the intrinsic ferroelectricity of specific 2D layered materials has been confirmed theoretically and experimentally, where the van der Waals interlayer interactions provide a new opportunity to avoid the problems above.[39–42] For example, in 2016, Liu et al. first reported the reversible out-of-plane (OOP) ferroelectricity in 4 nm $CuInP_2S_6$, with a Curie temperature (T_c) of 320 K.[43] In the same year, Chang et al. discovered the stable in-plane (IP) polarization of SnTe at the limit of 1 unit cell thickness, with a T_c of 270 K.[44] In 2017, a kind of 2D III_2–VI_3 compound In_2Se_3 was predicted to have robust ferroelectricity at the monolayer limit by Zhu et al.[45] Soon, experiments successfully synthesized the nanoscale-thin In_2Se_3 films and proved the robust ferroelectricity with a T_c of 700 K, which is much higher than room temperature.[46–51] Therefore, 2D In_2Se_3 has attracted widespread attention as soon as it was reported. As shown in Figure 2A, the number of published papers (searched using the keywords "two-dimensional/2D In_2Se_3" in the Web of Science database) increases rapidly and continuously since 2017, although the outbreak of the COVID-19 has severely hindered the

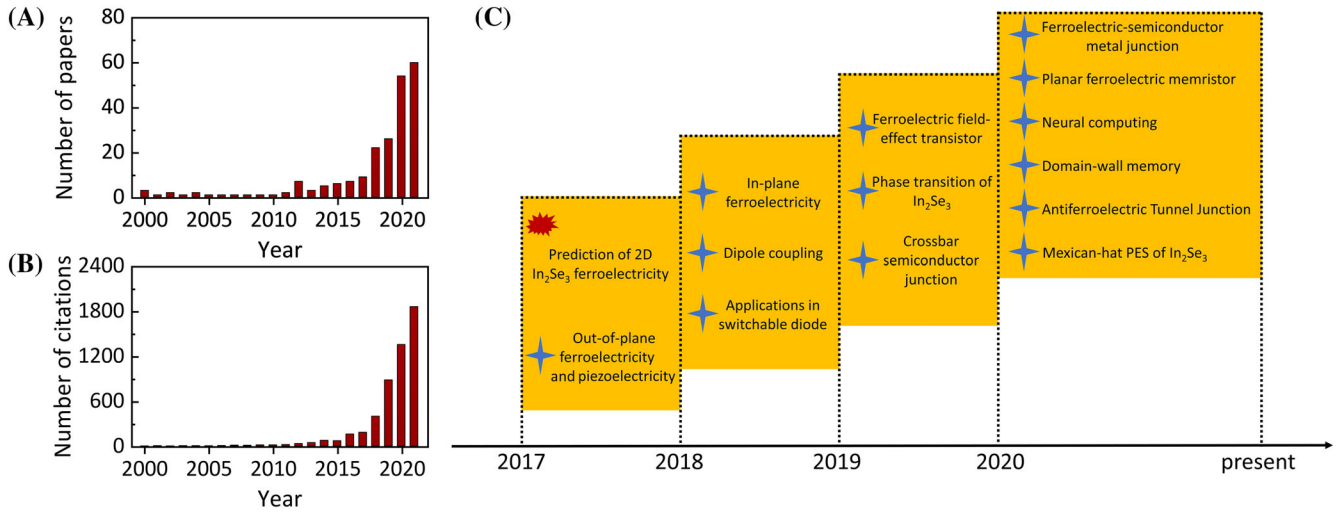

FIGURE 2 The number of papers (A) and citations (B) searched for the keyword "2D In_2Se_3/two dimensional In_2Se_3" in the Web of Science database in 2022. (C) Some breakthroughs/representative progresses on 2D In_2Se_3 ferroelectric material since 2017

progress of scientific research in the world. Figure 2B shows the citation number of the papers in Figure 2A, which also exhibits a sudden increase since 2017. Figure 2C summarizes some of the representative progresses in the investigation of 2D In_2Se_3, including the prediction of its ferroelectricity and the demonstration/characterization of its structures and properties.[45–53] After 2018, 2D In_2Se_3 was gradually applied to synaptic ferroelectric semiconductor junctions, ferroelectric semiconductor field-effect transistors, and memory-and-neural-computing system.[54–60] In_2Se_3 not only fills the gap of high-temperature 2D ferroelectrics, but also shows a great potential in the applications of high-density nonvolatile memory and neuromorphic computing, especially at the ultrathin scale.[54–60]

Although 2D In_2Se_3 has shown attractive properties and a great potential in the applications of ferroelectric devices, atomic structures of the related phases, and dynamic mechanisms of the ferroelectric switching are still controversial.[45,50,52] As a result, the optimization of their device performance faces challenges, for example, the miniaturization, speed, retention, reliability, and endurance still need further improvements for practical industrial applications.

In this review, we focus on the atomic pictures of different phases of 2D In_2Se_3, the dynamic processes of transitions between the key phases, the mechanism of ferroelectric switching, and the latest progresses in data memory/computing electronic devices based on 2D In_2Se_3. The relationships between material structures, properties, and device performance are also analyzed and discussed in detail. Finally, we summarize the problems, challenges, and outlooks of the material and its devices for data storage. We expect this review will be helpful and timely for the research community to better understand the mechanism and facilitate the development of 2D In_2Se_3 based advanced data storage applications.

2 | ATOMIC STRUCTURE OF 2D In_2Se_3

Atomic structure is the origin of material properties. Understanding the atomic picture of 2D In_2Se_3 can explain why it can resist the depolarization field as well as retain the ferroelectricity even at a monolayer limit, also can help to understand the process of its ferroelectric switching, and facilitate the design of high-performance ferroelectric devices. In this section, we systematically summarize the reported ferroelectric and paraelectric structures of 2D In_2Se_3. Especially, the structural diversity of paraelectric phases is discussed and explained in detail.

2.1 | α phase of 2D In_2Se_3

The α phase of 2D In_2Se_3 exhibits room-temperature ferroelectricity with spontaneous polarization in both OOP and IP directions.[45] Although the structure of bulk In_2Se_3 has been investigated by experiments for a long time,[61,62] the detailed picture of the α phase was not fully figured out until Ding et al found its lowest energy structure by first-principles calculations in 2017.[45] As shown in Figure 3, a monolayer In_2Se_3 consists of five subatomic layers arranged in an order of Se–In–Se–In–Se. These sublayers mainly have three types of locations in form of triangular grids marked with A, B, and C shown in Figure 3A.[45,63,64] The striking character of the α phase is that its two In sublayers hold two different local configurations including one for tetrahedral coordination (top In site) and another one for octahedral coordination (bottom In site), see Figure 3B. It is this inequality that leads to ferroelectricity (see Figure 3C). Naturally, the α In_2Se_3 with the opposite ferroelectric polarization is shown in Figure 3D. The OOP polarization also accompanies an IP polarization, and the polarizations in these two directions are locked to each other, as indicated by red and black arrows in Figure 3C,D. Such an atomic arrangement is further confirmed by later experimental observations via high-angle annular scanning transmission electron microscopy (STEM), selected area electron diffraction (SAED), and Raman spectra.[49–51,65,66] Moreover, the SAED patterns show that two kinds of diffraction spots can be observed in the few-layer α In_2Se_3, corresponding to 2H and 3R stacking α In_2Se_3, respectively. Raman spectra also show that the intensity of the E^2 mode of 2H α In_2Se_3 is stronger than that of 3R α In_2Se_3, which can be used as a criterion to distinguish the two structures.[51,65,66] The bulk In_2Se_3 is a layered material with van der Waals interactions. Therefore, α-phase 2D In_2Se_3 can be fabricated by the exfoliation method or the van der Waals epitaxial growth method.[67–70]

2.2 | β phase family of 2D In_2Se_3 and the diversity

The paraelectric phase of In_2Se_3, called β phase, with the $R\bar{3}m$ space group has an inversion symmetry structure with the central layer Se atom locate at the centrosymmetric position,[45,62,63] as shown in Figure 3E. Compared with the situation of α phase, in β phase both the two In sublayers hold the same octahedral configuration and the energy is 0.145 eV higher per unit cell.[71] This indicates the chemical bonding between In and middle-layer Se [Se(m)] atoms in 2D In_2Se_3 is relatively flexible. Due to the structural equality of the two In sublayers, the β

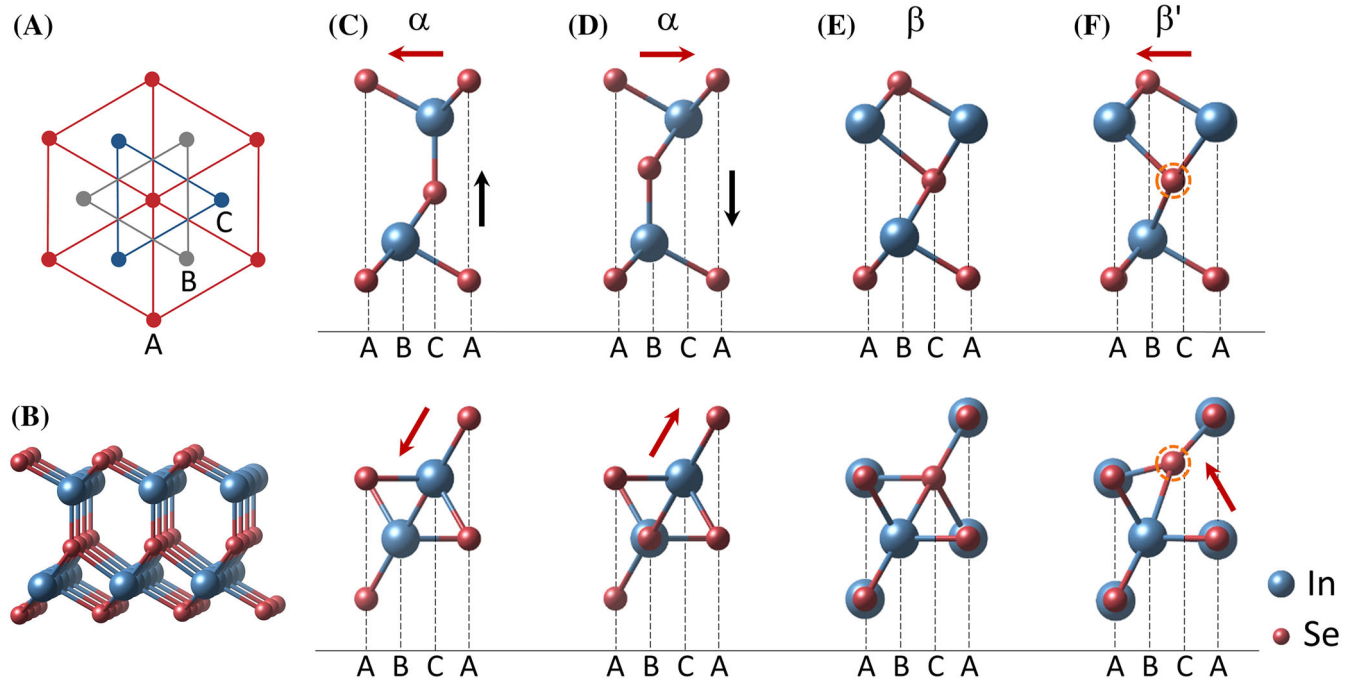

FIGURE 3 The structures of 2D In_2Se_3 obtained by first-principles calculations. (A) Top view of the crystal structure of monolayer In_2Se_3. Each layer of In_2Se_3 contains only one element, and the atoms in each layer are located at one of the A, B, and C sites. (B) 3D structure of α phase with upward polarization. (C–F) Side and top views of ferroelectric α phase with different polarizations, paraelectric β phase, and distorted β′ phase, respectively. The red and black arrows mark the directions of in-plane (IP) and out-of-plane (OOP) polarizations, respectively. Reproduced with permission.[45] Copyright 2017, Springer Nature

phase is paraelectric, which is in contrast to the ferroelectricity in the α phase. The paraelectricity and centrosymmetry of the β phase have been confirmed by low-energy electron microscopy (LEEM) and second-harmonic generation (SHG) experiments.[50,52] However, the phonon spectrum evaluated by first-principles calculations demonstrated this centrosymmetric β phase has significant imaginary frequencies and thus in fact is dynamically unstable.[45,72] One suggests that to eliminate the imaginary frequencies, Se(*m*) atoms should distort away from the centrosymmetric positions in the same direction and then form a new β phase named β′ (shown in Figure 3F).[45] The energy of β′ phase is 0.064 eV per unit cell higher than that of α phase, but 0.081 eV per unit cell lower than that of β phase.[45,71] Moreover, combing scanning tunneling microscopy, STEM, and density-functional theory (DFT) calculations, Zhang et al. revealed another kind of Se(*m*) distorted β phase in a form of the $2 \times \sqrt{3}$ reconstruction below 77 K. Its energy can be further lowed by 0.033 eV per unit cell than that of β′ phase.[73–76] In other words, the diversity of β related phases should be an important fingerprint in 2D In_2Se_3.

In 2021, by first-principles calculations and molecular dynamics (MD) studies, Huang et al. studied the physics behind and revealed a Mexican-hat potential energy surface (PES) which should be the origin of the diversity of β related structural phases.[72] As shown in Figure 4A, compared with the top [Se(*t*)] and bottom [Se(*b*)] layer Se atoms with single well PESs, the PES of the Se(*m*) atom of β In_2Se_3 exhibits a unique Mexican-hat profile. In this case, the Se(*m*) atoms will deviate from the centrosymmetric position (energy maximum) and fall into one of the 12 energy minima in the basin of the Mexican-hat PES.[72] As such, different phases can exist depending on the pattern of distortion of Se(*m*) atoms, such as the β′ phase discussed above.[52] In fact, the formation of these phases also depends on environmental conditions, such as temperature, substrate, and fabrication processes.

Another β phase, that is, the pseudo-centrosymmetric phase (β_{pc}) of 2D In_2Se_3, is further revealed based on the Mexican-hat PES.[72] As is shown in Figure 4A, due to the small energy barriers among the 12 positions with energy minima, it is difficult for In_2Se_3 to exist in the form of the aligned IP polarized β′ phase. Therefore, the β phase at a finite temperature is more inclined to be with a random distribution of Se(*m*) atoms in the basin of the Mexican-hat PES. Further, MD simulation at 750 K was carried out to investigate such a temperature effect. As the snapshot at one moment and the corresponding relaxed structures are shown in Figure 4B, the Se(*m*) atoms prefer to be randomly located in different off-center positions rather than in the central or a unified off-center site.[72]

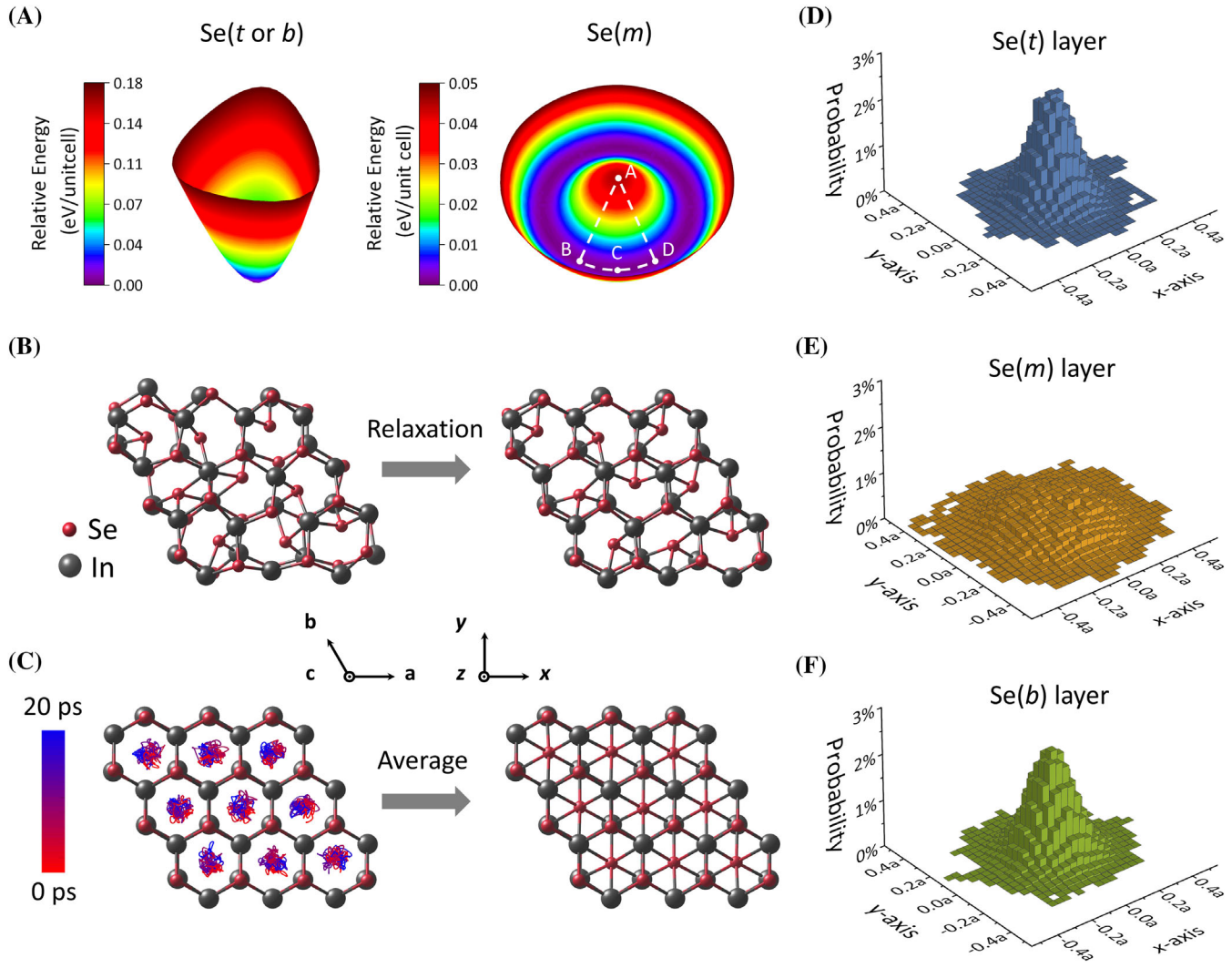

FIGURE 4 Characterization of 2D β In_2Se_3 through first-principles calculations. (A) Potential energy surfaces of Se atoms in different layers in the IP direction. (B) Snapshot (left) and the relaxed structure (right) of β phase during the 750 K molecular dynamics (MD). (C) Trajectories of the middle layer Se atoms and the average structure of the β phase during 20-ps MD at 750 K. (D–F) Distribution probabilities of Se atoms in different layers during 20-ps MD at 750 K. Reproduced with permission.[72] Copyright 2021, AIP Publishing

The structures in Figure 4C show that the time-averaged effect of the β phase is equivalent to a centrosymmetric phase during the 20-ps MD simulation, indicating that the centrosymmetric phase observed by the SHG experiment is highly possible a result of the time-averaged effect of the random distortion of Se(*m*) atoms.[50] Thus, they named it the β_{pc} phase. Figure 4D–F show the real-space distribution probability of Se atoms in different layers during the 20-ps simulation. The distribution probabilities of the Se(*t*) and Se(*b*) atoms are quite sharp, while that of the Se(*m*) atoms is really flat, which matches to their PES profiles perfectly in Figure 4A. Such a β_{pc} phase can be retained even when the temperature is quenched to room temperature according to the MD simulation.[72] The existence of the β_{pc} phase can play a significant role in the ferroelectric switching behavior of 2D In_2Se_3, which will be discussed later in Section 4.2. Interestingly, the Mexican-hat PES is proved to be a general physical phenomenon in the family of 2D III_2–VI_3 ferroelectric materials. Therefore, the pseudo-centrosymmetric atomic picture at raised temperatures is also applicable to all 2D III_2–VI_3 materials.[72]

Table 1 summarizes the structural information of typical phases of In_2Se_3. Here, we try to summarize the structural features of 2D In_2Se_3. As seen in α In_2Se_3 (Figure 3B), a Se(*m*) atom bonds with four In atoms: one top-layer In atom [In(*t*)] and three bottom-layer In atoms [In(*b*)]. In this case, In_2Se_3 holds an upward polarization. To reverse the polarization, the chemical bonds must first be broken and reformed in the form of Se(*m*) atom bonding to one In(*b*) atom and three In(*t*) atoms. On the other hand, the lateral slides of five atomic layers are required

TABLE 1 Crystal structures and ferroelectricity of In_2Se_3

In_2Se_3	Crystal structure	Lattice parameters (Å)	Ferroelectricity	References
α (monolayer)	R3m	$a = b = 4.11$	IP and OOP	[45,50]
α (2H) (bulk)	$P6_3mc$	$a = b = 4.05$ $c = 19.75$	Layer dependent	[66]
α (3R) (bulk)	R3m	$a = b = 4.06$ $c = 29.64$	IP and OOP	[66]
β (monolayer)	$R\bar{3}m$	$a = b = 4.00$	Non	[63]
β (1T) (bulk)	$P\bar{3}m1$	$a = b = 4.04$ $c = 9.76$	Non	[66]
β (2H) (bulk)	$P6_3mc$	$a = b = 4.06$ $c = 19.48$	Non	[66]
β′ (monolayer)	Anisotropic stripe fcc′ structure	$a = b = 4.05$	IP	[45,73]
β ($2 \times \sqrt{3}$) (monolayer)	$2 \times \sqrt{3}$ reconstruction from β	$a = 8.14 \pm 0.17$ $b = 7.02 \pm 0.10$	IP	[73,74]
β_{pc} (monolayer)	Pseudo-centrosymmetric structure	—	Non	[72]
γ	$P6_1$	$a = b = 7.35$ $c = 20.02$	IP and OOP	[66,77]

Abbreviations: IP, in-plane; OOP, out-of-plane.

for the ferroelectric (α) to paraelectric (β) phase transition. The stable ferroelectricity of 2D α In_2Se_3 is attributed to its unique re-bonding mechanism and the locking between polarizations in the OOP and IP directions, rather than the long-range Coulomb interactions in conventional displacement-type ferroelectrics. Therefore, to eliminate the polarization, the Se(m) atoms must move significantly (~100 pm), accompanied by the re-bonding of the In—Se covalent bond.[45] In contrast, the elimination of polarization in conventional displacement-type ferroelectric materials requires only a small uniaxial atomic distortion (~10 pm) in the structure without bond re-configuration.[50] Therefore, the requirements of bond reconstruction and lateral slide in 2D In_2Se_3 make its ferroelectricity much more robust to resist the depolarization field even at its monolayer limit. To stress the differences between 2D III_2–VI_3 family and displacement-type ferroelectrics, here one may name them phase-change-type ferroelectrics.

3 | FERROELECTRICITY OF 2D In_2Se_3

2D ferroelectric materials with robust ferroelectricity were relatively rare before. Thanks to some pioneer works, such as the theoretical prediction of intrinsic 2D ferroelectricity in In_2Se_3 by Wenguang Zhu et al. in 2017, experiments start to focus on this topic.[45] Currently, both the predicted OOP and IP ferroelectricity of α In_2Se_3 have been verified experimentally.[46–51] The ferroelectricity is robust since the T_c can be as high as 700 K.[50,71] Moreover, the polarization switching driven by the electric field has also been experimentally confirmed.[46–50] All of these have laid an important foundation for the practical application of 2D In_2Se_3 ferroelectric.

3.1 | Out-of-plane ferroelectricity in α In_2Se_3

The ferroelectricity of materials is often accompanied by piezoelectricity,[78,79] which has the characteristic of lattice deformation under an external electric field or vice versa.[80] Therefore, ferroelectricity can be detected by applying a voltage to the surface of the sample through the piezoresponse force microscopy (PFM) probe.[81] In addition, local ferroelectric domain programming on the sample surface can be achieved by applying an electric field (from the tip of PFM) greater than the coercive field. As such, PFM imaging has become one of the most intuitive methods to verify ferroelectricity.

In 2017, Zhou et al. reported the experimental evidence of the OOP polarization in 2D and quasi-2D In_2Se_3.[46] Figure 5A shows the atomic force microscopy (AFM) image of the >100 nm-thick In_2Se_3 flake with smooth terraces. The corresponding PFM phase and amplitude images are shown in Figure 5B,C. It can be seen that there are two areas with opposite phase contrast of 180° in Figure 5B, corresponding to the upward and downward OOP polarizations, respectively. The dark lines in Figure 5C are the domain walls of two polarized regions with opposite directions. They also investigated ferroelectric polarization in thinner α In_2Se_3 flakes with thicknesses ranging from 3 to 60 nm, which were prepared on a gold substrate by mechanical exfoliation. Figure 5D–F shows the AFM image, PFM phase image, and PFM amplitude image, respectively. The numbers 1–6 in

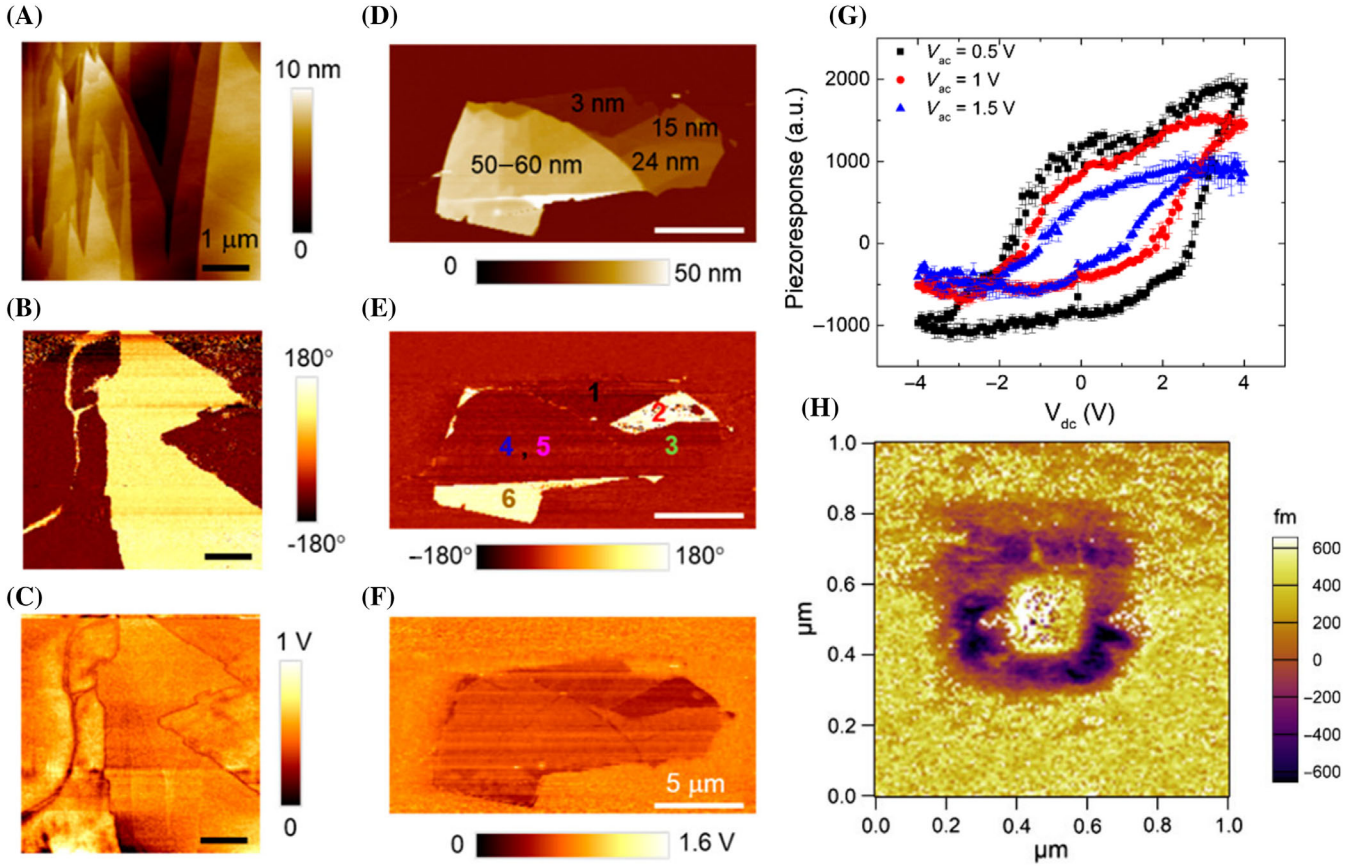

FIGURE 5 Experimental characterization of the OOP polarization of α In_2Se_3. (A) Atomic force microscopy (AFM) image of >100 nm thick α In_2Se_3 flake prepared by mechanical exfoliation (scale bar, 1 μm). (B) The OOP piezoresponse force microscopy (PFM) phase image and (C) the corresponding amplitude image, domains with a phase difference of 180° represent opposite polarizations (scale bar, 1 μm). (D–F) AFM image, OOP PFM phase and amplitude images of thinner α In_2Se_3 with thickness range from 3 to 60 nm (scale bar, 5 μm). Reproduced with permission.[46] Copyright 2017, American Chemical Society. (G) OOP piezoresponse of 3 nm thick α In_2Se_3 during polarization reversal. (H) PFM image of domains that are electrically written by opposite voltage, the positive write voltage of +6 V is applied to the inner box, while the applied voltage of the outer box is −6 V. Reproduced with permission.[50] Copyright 2018, American Physical Society

Figure 5E correspond to the areas with different thicknesses in Figure 5D. Clear domains with a phase difference of ~180° are observed in Figure 5E, demonstrating the robust OOP ferroelectricity at room temperature.[46] On the other hand, in 2018, Xiao et al. demonstrated that the OOP ferroelectricity of α In_2Se_3 has a T_c of 700 K by monitoring the change of SHG signal intensity with increasing temperatures.[50]

The ability to switch ferroelectric polarization under an electric field is a key requirement for practical applications of ferroelectrics. The polarization switching of 2D α In_2Se_3 has been verified by some experiments.[46–50] For example, Xiao et al. investigated the switching of OOP polarization of a trilayer α In_2Se_3 flake by applying an external electric field at room temperature.[50] Figure 5G shows that the piezoresponse of In_2Se_3 exhibits a hysteresis loop as the external perpendicular poling voltage changes.[50] In Figure 5H, by applying an electrically biased scanning probe, the quadrate domains with opposite piezoresponse were written. Due to the absence of ultrafast time-resolved detections, the speed of such ferroelectric switching has not been systematically studied.[50] The evolution of domain-wall structure and movement during the switching also needs further investigations.

3.2 | In-plane ferroelectricity in α In_2Se_3

As suggested by the IP structure asymmetry from the different positions of the top and bottom layer In atoms, α In_2Se_3 also shows IP ferroelectricity. In 2018, through chemical vapor deposition (CVD) method, Cui et al. successfully synthesized nano-thick In_2Se_3 on mica substrate.[49] Figure 6A shows the topographic image of the α In_2Se_3 sample with a thickness of 2–6 nm. The corresponding IP PFM images are shown in Figure 6B,C.

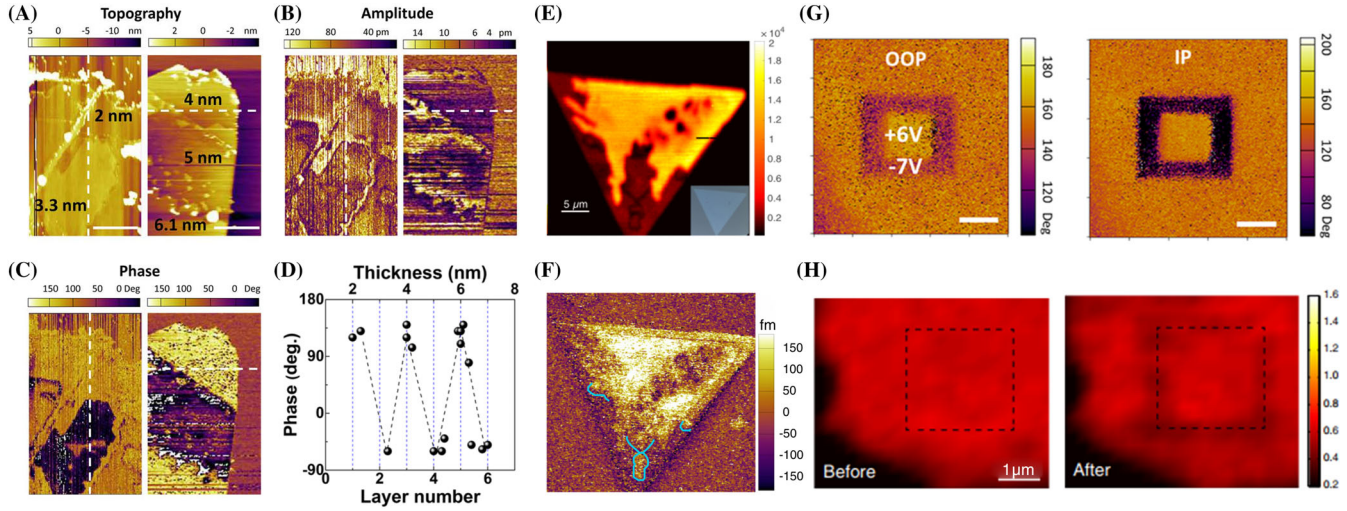

FIGURE 6 Experimental characterization of the IP polarization of 2D α In_2Se_3 by PFM and second-harmonic generation (SHG). (A) AFM images of 2–6.1 nm thick α In_2Se_3 flake (scale bar, 1 μm). (B,C) The corresponding IP PFM amplitude and phase images. (D) The evolution of the IP PFM phase with the thickness/layer of the flake. Reproduced with permission.[49] Copyright 2018, American Chemical Society. (E) SHG mapping of 3 nm thick α In_2Se_3, the strength of the SHG signal represents the strength of the polarization (scale bar, 5 μm). (F) The corresponding piezoresponse mapping, which matches well with the SHG signal in (E). Reproduced with permission.[50] Copyright 2018, American Physical Society. (G) OOP (left) and IP (right) PFM phases images of two squares polarized with +6/−7 V tip voltage. The direction of the IP polarization changes correspondingly with the change of the OOP polarization, showing the correlation effect of polarization (scale bar, 1 μm). Reproduced with permission.[49] Copyright 2018, American Chemical Society. (H) IP SHG mappings of In_2Se_3 before and after the PFM reverse polarization, the region enclosed by the square dashed line corresponds to the area where the polarization is switched. The black line at the edge of the polarization inversion region in the right figure is the result of destructive interference, indicating that the IP polarization is inverted under the action of the OOP electric field. Reproduced with permission.[50] Copyright 2018, American Physical Society

Both the amplitude and phase images indicate that the ferroelectric domains are formed in each thickness region. Interestingly, the direction of the ferroelectric polarization strictly depends on the number of layers. As shown in Figure 6D, the PFM phases of odd-layer and even-layer In_2Se_3 show a difference of 180°, indicating that the polarization directions are opposite. The asymmetric bonding configuration breaks the structural symmetry of monolayer α In_2Se_3 in both IP and OOP directions, resulting in coupled ferroelectric polarization in these two directions. In multilayer α In_2Se_3, the directions of the IP polarization of adjacent layers are the same for the 3R stacking sequence but opposite for the 2H stacking sequence. As such, the IP and OOP polarizations are preserved in multilayer α In_2Se_3 with a 3R stacking sequence. For 2H α In_2Se_3, the total IP polarization depends on the number of layers. In 2020, Lv et al. also verified the layer-dependent effect of ferroelectricity in few-layer 2H α In_2Se_3.[82] They calculated the magnitude of the ferroelectric polarization of 2H α In_2Se_3 of different thicknesses and confirmed that the IP electric dipole is always about 2.18 eÅ in the odd-number layers, while in the even-layers, the value is almost zero. A similar phenomenon was also observed in their PFM phase images, which further confirms the even-odd layer-dependent IP polarization ferroelectricity of 2H α In_2Se_3.[82] First-principles calculations also suggest that the 2H structured multilayer α In_2Se_3 is energy favorable.[49]

Besides the PFM measurement, SHG is another effective method to investigate the ferroelectricity of materials. When detecting a sample with broken symmetry, it can generate a signal with a frequency that is twice the incident frequency.[83] Combining the SHG and PFM mapping, Xiao et al. revealed the relationship between the ferroelectricity and the asymmetry of In_2Se_3 at room temperature.[50] As shown in Figure 6E,F, the intensity of the SHG signal mapping and the piezoresponse of the PFM correspond to each other. To be specific, the larger the piezoresponse amplitude (Figure 6F), the stronger the SHG signal (Figure 6E), that is, the greater the IP structure asymmetry. By comparing the OOP and IP intensities of angle-dependent SHG, they identify that the IP dipole is one order of magnitude larger than the OOP dipole.[50] Note that the strong IP polarization of 2D α In_2Se_3 also can provide a platform for memristive devices and neuromorphic devices.

In fact, the switching of the IP ferroelectricity is interlocked with the switching of the OOP ferroelectricity. As

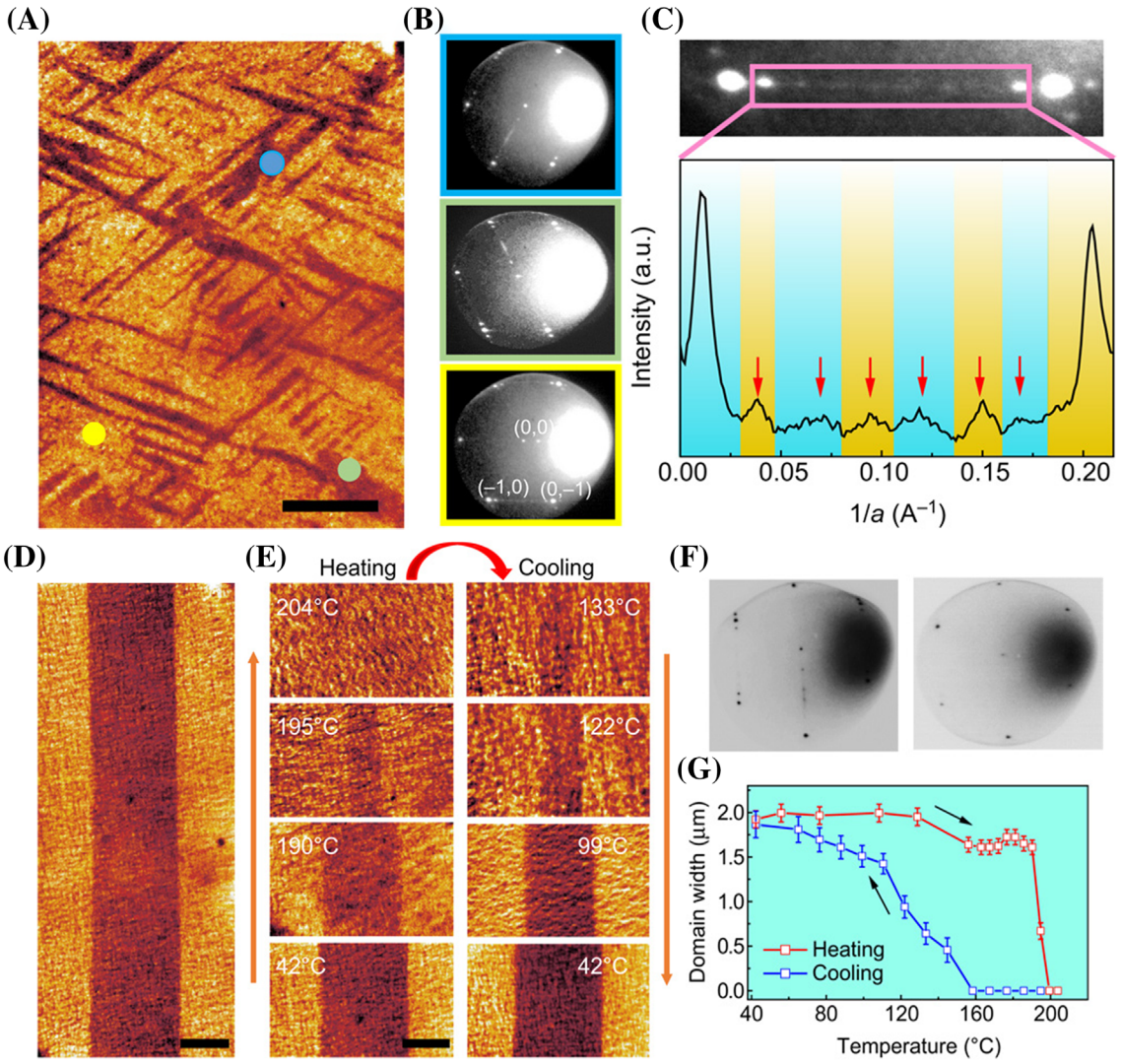

FIGURE 7 Characterization of the IP polarization and ferroelectric transition of β′ In_2Se_3. (A) Bright-field low-energy electron microscopy (LEEM) image of β′ In_2Se_3 (scale bar, 1.5 μm). (B) Micro-low-energy electron diffraction (μ-LEED) patterns of the three domains marked by blue, green, and yellow dots in (A). (C) Diffraction intensity curve between (−1,0) and (0,−1) subspots in (B). (D) LEEM image of a 1.9 μm width domain at room temperature (scale bar, 1 μm). (E) Evolution of the domain in (D) as the temperature increases and decreases (scale bar, 1 μm). (F) μ-LEED pattern of β′ In_2Se_3 at (left) 109°C and (right) 204°C. (G) The evolution curve of the domain width in (E) as a function of temperature. Reproduced with permission.[52] Copyright 2018, American Association for the Advancement of Science

shown in the atomic structures in Figure 3, the upward polarization is interlocked with the leftward polarization, while the downward polarization is interlocked with the rightward polarization. Indeed, Cui et al. programmed two square domains with opposite vertical tip voltages (+6 and −7 V, respectively) and observed that the OOP PFM phase image agrees well with the IP phase image (see Figure 6G).[49] Such a correlation is also observed by Xiao et al. As shown in Figure 6H, after the OOP electric field patterning, the IP SHG signal can still be detected in the programmed area (enclosed by the dashed line). In addition, a dark line caused by destructive interference appears at the dashed boundary, which proves that the OOP polarization reversal is accompanied by the IP polarization reversal.[50] Therefore, IP ferroelectricity can also be controlled by the OOP electric field. The interlocked IP and OOP polarization discussed here should be a general feature of phase-change-type III_2–VI_3 ferroelectric materials, which enables them to resist depolarization field even when the thickness is reduced to the 2D limit.[45]

3.3 | In-plane ferroelectricity in β′ In_2Se_3

The β phase with centrosymmetric configuration was considered as the paraelectric phase of In_2Se_3 in the past few decades.[62] It is generally accepted that the

centrosymmetric β phase can be obtained by raising the temperature of the ferroelectric α phase above the T_c.[85–87] However, as mentioned in Section 2, the β′ phase (with Se(m) distorted in the same direction) has lower energy than the β phase.[45,71] In addition, the distortion of the Se(m) atoms in the β′ phase will undoubtedly induce IP ferroelectricity. In 2018, using LEEM, Zheng et al. confirmed the room temperature IP ferroelectricity of β′ In_2Se_3 with thicknesses ranging from bulk to 45 nm.[52] Blue, green, and yellow dots in Figure 7A mark the three kinds of domains of β′ phase measured by bright-field LEEM at room temperature. The corresponding Bragg diffraction spots are given in Figure 7B. It can be seen that there is a row of subspots along one of the three equivalent directions in each domain, which means that the ferroelectric polarization is formed along these three equivalent directions. The intensity profile in Figure 7C shows that the distance between two main diffraction spots is equally divided into nine parts by the subspots, indicating that the period of each domain as nine primitive cells.[52]

Due to the small energy difference between β′ and paraelectric β phases, temperature elevation can "melt" the order of the β′ phases and transform it into the β phase.[52] The LEEM and low-energy electron diffraction revealed the real-time imaging of the β′ ↔ β phase transition in real space and reciprocal space, respectively.[52] Figure 7D shows a long ferroelectric domain with a width of 1.9 μm at room temperature. As the temperature increased from 42 to 190°C, the width of the domain slightly shrank to 1.6 μm (see Figure 7E). When the temperature rises to 195°C, the width of the domain dramatically shrinks to 0.67 μm and finally disappears at 204°C. The corresponding reciprocal space images in Figure 7F also show that the sub-diffraction points disappear after the transition, which means the "melting" of the IP polarized superstructure. On the contrary, when the temperature of the sample is re-cooled to 42°C, the domain with a width of 1.9 μm will eventually be restored, as shown in Figure 7E (right). It is worth noting that the domain wall appears at its original position, suggesting a memory effect after the reversible transition.[52] One possible explanation is that there are remained domain structures outside the observed region, which act as the seeds for the nucleation of domains during cooling. The evolution of the ferroelectric domain width during heating and cooling processes were summarized in Figure 7G. A hysteresis loop can be observed, indicating different dynamic processes between the forward and backward transitions.[52] In addition, the authors also confirmed the existence of stable IP ferroelectricity of the β′ phase in an atmospheric environment at room temperature by PFM and pointed out that the T_c of β′ phase to paraelectric β phase is 200 °C.[52]

4 | ATOMIC-SCALE STUDY OF FERROELECTRIC SWITCHING OF 2D In_2Se_3

Ferroelectric switching between two polarization states is the basis of the functionality of ferroelectric memory or computing devices, such as FeRAM and FeFET. Moreover, structural transitions between different phases not only act as intermediate processes of ferroelectric switching, but also directly influence the performance of these devices. Therefore, understanding the microscopic mechanism of ferroelectric switching and phase transitions of In_2Se_3 is a prerequisite for designing, controlling, and optimizing related devices.

For bulk In_2Se_3, its phase transitions have been widely investigated. As early as 1957, through electrical conductivity and thermal expansion analyses, Miyazawa et al. reported the first-order phase transition from α to β at 200°C.[85] Subsequently, a large number of investigations on phase transitions based on X-ray diffraction, transmission electron microscope, and electrical property measurements have sprung up. These researches reveal a complex phase diagram of bulk In_2Se_3, including the low-temperature α′ phase, the room temperature α phase, and the high-temperature (>60°C) β, γ, δ phase.[61,62,77,86–94] The existence of so many metastable phases also suggests the flexibility of chemical bonds in In_2Se_3. Recently, due to the discovery of the robust ferroelectricity of 2D α In_2Se_3,[45] the phase transitions in its 2D limit attract much attention. However, limited by the difficulty of the time-resolved and in-situ experimental detections at the atomic scale, the ferroelectric switching phase transitions between different phases of 2D In_2Se_3 are still not fully understood. Here, we summarize some theoretical investigations that provide possible pictures for the ferroelectric switching in 2D In_2Se_3.

4.1 | Theoretical prediction of the pathway of the polarization reversal process

In 2017, Ding et al. predicted the transition between the two α phases with opposite polarized states by first-principles calculations.[45] They proposed two possible pathways for the polarization reversal. In terms of atomic structure, the 2D In_2Se_3 with different polarization directions differ only in the position of the Se(m) atom. Therefore, the first method is to directly shift the Se(m) atom from the downwardly polarized site to the upwardly polarized site (named single-step method), as shown in Figure 8A. The calculated energy barrier is 0.85 eV per unit cell. The second pathway (found by the climbing

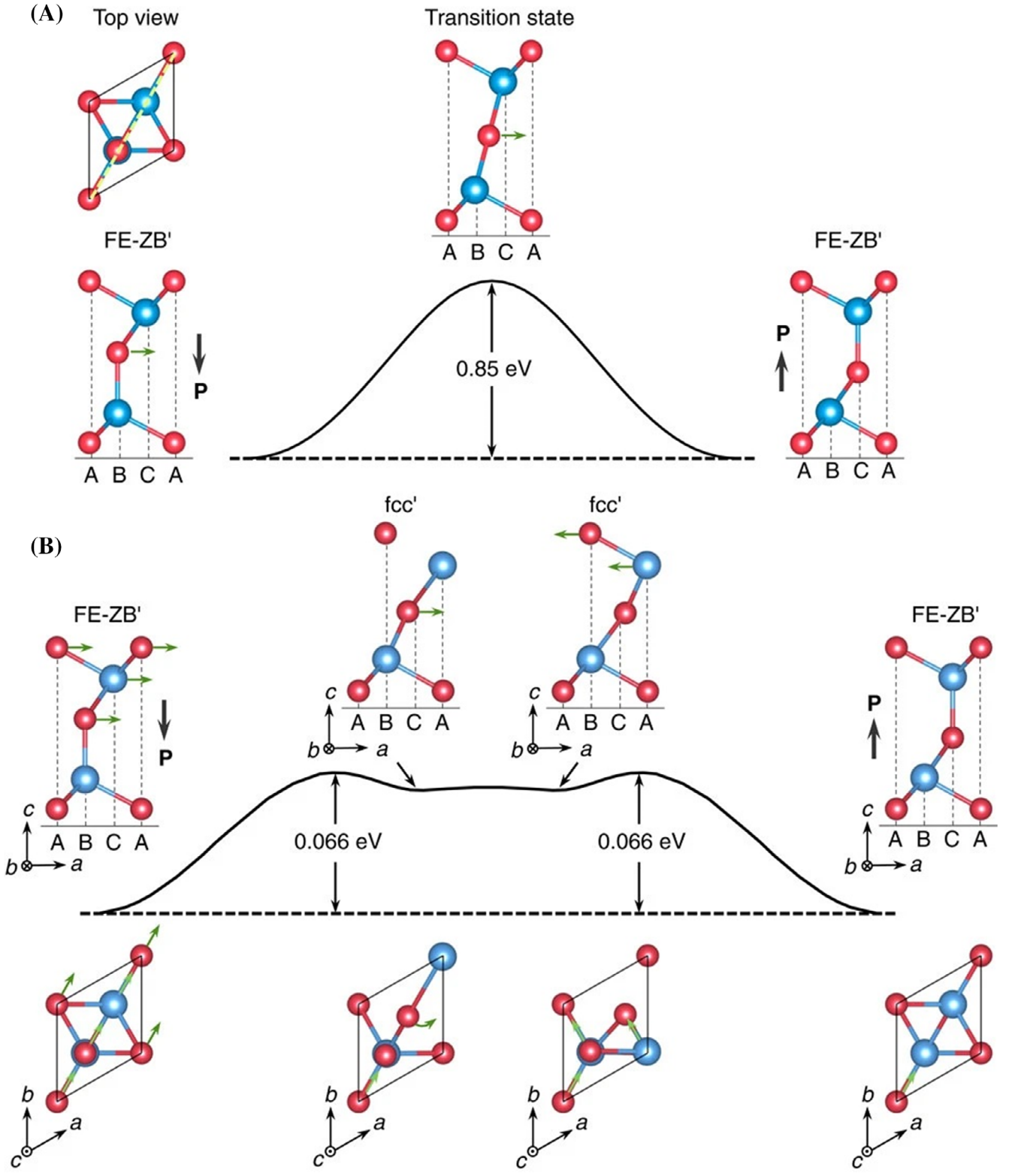

FIGURE 8 Pathways and energy barriers for the polarization reversal process in 2D α In_2Se_3. (A) The middle layer Se atom moves directly from the downwardly polarized site to the upwardly polarized site, and the other four atoms remain fixed. The energy barrier for the transition is 0.85 eV per unit cell. (B) Another energetically favorable three-step concerted reversal mechanism. The activation barrier is effectively reduced to 0.066 eV per unit cell. Reproduced with permission.[45] Copyright 2017, Springer Nature

image nudged elastic band method) contains three steps (named three-step method), as shown in Figure 8B. The first step starts with the downwardly polarized α phase, the upper three layers move collectively in the same direction and form a typical β′ structure. In the second step, the central layer Se atoms rotate 60° around the C site and form another degenerate β′ phase. For the last step, only the upper two layers move collectively in a direction that rotates 60° counterclockwise in the original movement direction and finally transforms into the α phase with upward polarization. The calculated highest energy barrier of the three-step transition process is only 0.066 eV per unit cell, which is one order of magnitude lower than the 0.85 eV per unit cell of the single-step method.[45] As such, the second pathway should be more promising. However, how to ensure the one-by-one collective movements of the three-step method to realize the ultrafast switching process dynamically is still an open question.

4.2 | Theoretical MD simulation of the ferroelectric transition

In 2018, Liu et al. simulated the ferroelectric-to-paraelectric transition of 2D In_2Se_3 by ab initio MD.[71] The authors simulated the magnitude of the IP and OOP polarizations at various temperatures ranging from 0 to 1500 K through MD and confirmed that the T_c of 2D In_2Se_3 is 700 K, which is consistent with the experiment.[50] Furthermore, MD simulation showed that the transition from ferroelectric to paraelectric phase can be completed within 1.5 ps. The ultrafast transition is attributed to the relative collective motions of the upper three and lower two atomic layers of In_2Se_3, which is consistent with the first step of the three-step method discussed in Section 4.1. It can be obtained from MD that the ferroelectric transition is accompanied by a decrease in energy of 0.2 eV per unit cell. Given the fact that the free energy of α phase at 0 K is slightly lower than that of β phase,[45] the reduction in the total energy at high temperatures may be related to the entropy, or the atomic structures of α and β phases at high temperature is somewhat different from those at 0 K. Further insightful investigations are needed.

In 2021, through MD simulations and phonon projection analyses, Huang et al. found that the collective motion between atomic layers during the ferroelectric-to-paraelectric transition is induced by the IP shear phonon mode of α phase activated at high temperature.[72] Figure 9A,B shows the atomic structure of 2D In_2Se_3 before and after 4-ps MD simulation at 750 K. The atomic structure changes from α to β, which indicates the ferroelectric-to-paraelectric transition has been completed. The corresponding atomic displacements in Figure 9D,E quantitatively describe the relative IP displacements among different atomic layers during the transition. The results show highly consistent displacements between In(*t*) and Se(*t*) atoms or between In(*b*) and Se(*b*) atoms, while the displacements of Se(*m*) atoms are related to those of the bottom two layers, but to a smaller degree. These results reflect the highly coherent motion of atoms, that is, atoms in the upper two layers and atoms in the lower three layers move in opposite directions during the phase transition. Further, through phonon projection analysis, the authors found that it is the activation of an IP shear phonon mode of 2D α In_2Se_3 at high temperature that triggers the coherent motion among atomic layers. As shown in Figure 9F, the displacements of most phonon modes oscillate near zero as time evolves, only the IP shear phonon mode evolves monotonically from zero to a positive displacement value. The arrows in Figure 9C show the vibration directions of this IP shear phonon mode. As we can see, the relative displacement among atomic layers is consistent with the theoretical prediction in Section 4.1 and the results of the MD simulations above, indicating that the ultrafast α-to-β transition is a result of excitation of the IP shear phonon mode.[72]

The transition from α phase to β phase (α↑ to β in Figure 9) above is a part of the ferroelectric polarization reversion. Its ultrafast spontaneous dynamics indicate that it is a relatively easy process. On the other hand, the rest part of the polarization reversion, that is, the β-to-α transition (β to α↓), may be a more difficult process. Indeed, the existence of the pseudo-centrosymmetric β_{pc} phase with the random Se(*m*) distribution, which has been discussed in Section 2.2, provides a significant entropy barrier that prevents the reverse β-to-α phase transition from occurring coherently.[72] Therefore, it is hard to achieve ultrafast reversible ferroelectric phase transition unless the positions of the Se(*m*) atoms of the β phase remain consistent, that is, each Se(*m*) atom locates at the same minimum of the Mexican-hat PES as the case in β′ phase. To confirm this point, Huang et al. further performed β-to-α transition (β to α↓) simulations with β_{pc} and β′ phase being an initial structure, respectively. The results show that the reverse ferroelectric transition from β′ to α can happen within tens of picoseconds under an OOP electric field. However, at the same timescale, the β_{pc} phase remained stable and did not transform into the α phase.[72] The dynamics of a full process of the reversible ferroelectric switching under an electric field still need further studies. For a real sample with a finite size, the transition should also closely interact with domain-wall structures, which is also an important topic to be addressed in the future.

5 | ELECTRONIC DEVICES BASED ON FERROELECTRIC 2D In_2Se_3 FOR DATA STORAGE

Owing to the excellent property of 2D In_2Se_3, its various electronic devices are successfully fabricated soon after the theoretical prediction.[54–60,95–97] Although memory or computing devices based on ferroelectric materials were considered a promising technology, the problem of depolarization field that plagues ferroelectrics is particularly prominent in the era of device miniaturization for high-density data applications.[98] Now, the development of 2D In_2Se_3 will significantly promote the research of nanoscaled devices such as FeFETs, ferroelectric semiconductor channel field-effect transistors (FeS-FETs, also called FeCTs), ferroelectric memristors, and ferroelectric semiconductor junctions (FSJs).[54–57,96,99] Investigations on these devices not only demonstrate the practicability of 2D In_2Se_3, but also reflect the challenges and thus show the directions for future optimizations. In this section, we review the latest works on electronic devices based on 2D or quasi-2D In_2Se_3 for data storage-related applications. Some issues of device developments are also discussed.

5.1 | Ferroelectric gate based field-effect transistor

The FeFET is one of the most important applications of ferroelectrics due to its fast switching speed,[100–104] its

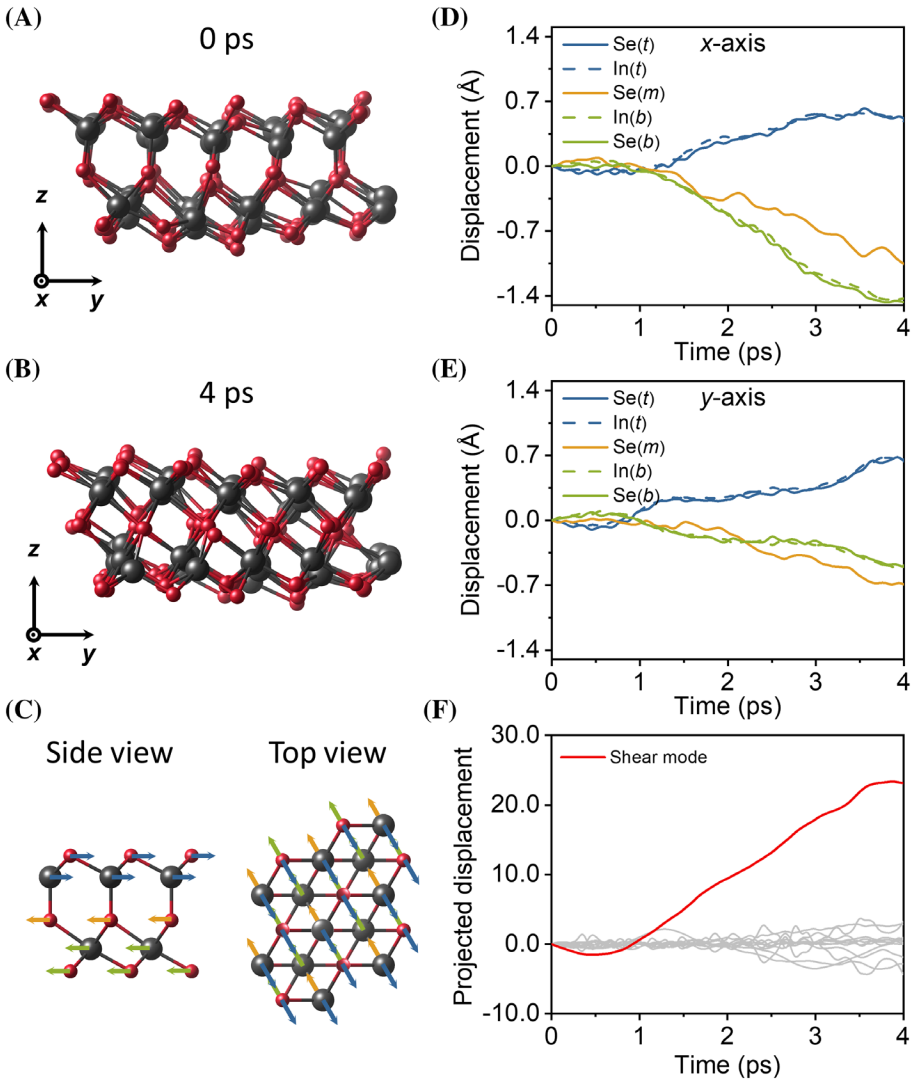

FIGURE 9 Molecular dynamics (MD) simulation of the transition from ferroelectric to paraelectric in 2D In_2Se_3 induced by shear phonon mode. (A) Initial and (B) final atomic structure of the 4-ps MD simulation at 750 K. (C) Schematic diagram of the shear phonon mode that triggers the ferroelectric transition of the α phase. (D,E) The displacements of atoms in different layers along the *x* and *y* directions during the 4-ps simulation. (F) Projection of atomic displacements on 12 optical phonon modes of the α phase during the 4-ps MD simulation. Reproduced with permission.[72] Copyright 2021, AIP Publishing

nondestructive readout process,[105–107] and its nonvolatile property.[108–113] In 2019, Wan et al. reported a 2D FeFET based on 2.6 to 70 nm thick α In_2Se_3.[54] The 3D schematic and optical images are shown in Figure 10A,B. The α In_2Se_3 served as a top-gate dielectric and the graphene was adopted as a conducting channel. The *h*-BN layer is added to improve the interface characteristics while enhancing the conductivity of graphene. By changing the top-gate voltage (V_{TG}), the ferroelectric polarization of α In_2Se_3 can be switched, therefore, different types of carriers would be induced or doped into graphene, resulting in the shift of the Fermi level and the modulation of resistance. Figure 10C shows that the transfer characteristic of the device exhibits a hysteresis loop, reflecting the ferroelectric nature of α In_2Se_3.[54] Points I and III are the two stable states where the electric dipoles of α In_2Se_3 are aligned with the corresponding external electric fields, and points II and IV are the maximum resistance states

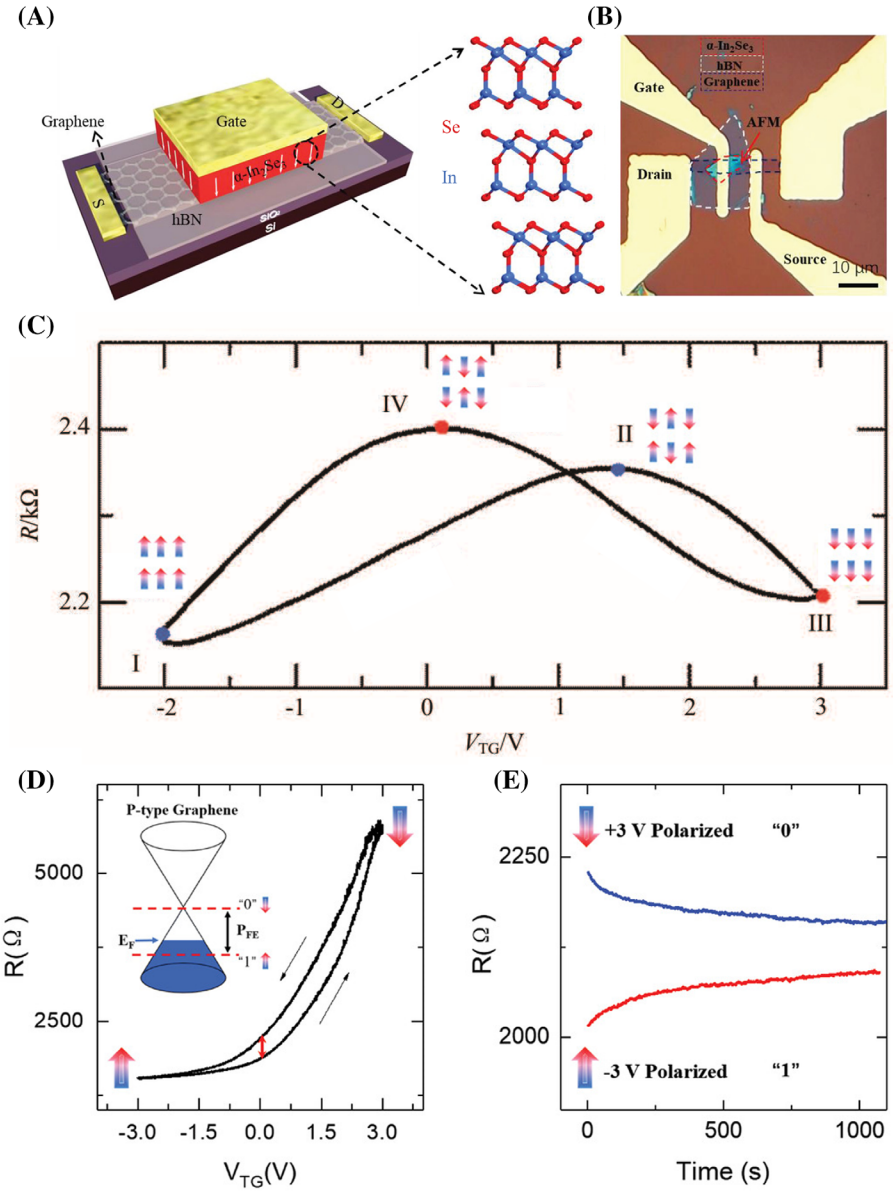

FIGURE 10 Structural and electrical characterizations of 2D In_2Se_3 FeFET. (A) Schematic diagram of the structure of FeFET, α In_2Se_3, *h*-BN, and graphene are vertically aligned from top to bottom. (B) The corresponding optical image of 2D FeFET (scale bar, 10 μm). (C) Transfer characteristic curve of the 2D FeFET device, the evolution of resistance exhibits a butterfly profile with the change of the top-gate voltage. (D) Transfer characteristic curve of the p-doped FeFET, the resistance increases or decreases monotonously during the polarization reversal process. E_F is the initial Fermi level of p-doped graphene, and the red dash lines are the final Fermi levels of graphene in two different polarization states of 2D In_2Se_3. (E) The retention performance of the p-doped FeFET device in (D). Reproduced with permission.[54] Copyright 2019, John Wiley and Sons

during the polarization reversal transition. In principle, the stable single upward and downward polarization states can be used to encode the logic bits 0 and 1 for memory or computing functionality. However, the butterfly-shaped curve in Figure 10C makes it difficult to distinguish the difference between the resistances of two stable polarized states ($R_{P\uparrow}$ and $R_{P\downarrow}$). To increase the resistance contrast, the authors used a heavily doped p-type graphene as conducting channel to achieve a monotonic change in resistance during the polarization reversal. As shown in Figure 10D, the resistance contrast $\frac{\Delta R}{R}$ (defined as $\frac{R_{P\uparrow}-R_{P\downarrow}}{R_{P\uparrow}+R_{P\downarrow}}$) has been effectively enlarged from 1% to 58.5%. The retention test of the p-FeFET device in Figure 10E shows that after the ±3 V polarizing, the resistances of the two polarization states are still distinguishable within 1000 s, which indicates a nonvolatility.[54] Also, the cyclic testing proves that after 10^5 erasing and writing, the device performance remains stable. However, compared with other memory technologies, such as phase-change memory or resistive memory,[114,115] the on/off ratio of this FeFET is relatively small (less than an order of magnitude), and the switching speed is still slow (about 50 ms).[54]

5.2 | Ferroelectric channel-based field-effect transistor

In traditional FeFET, ferroelectric materials serve as the gate to tune the electric conducting channel in adjacent semiconductors (see Figure 11A, up). Si et al. proposed that utilizing the semiconducting feature of In_2Se_3 (with a bandgap of 1.3–2.0 eV, depending on thickness),[49,63,68,88,116] it can also be used as the conducting channel, namely, FeS-FET (see Figure 11A, down).[55] Figure 11B shows a 3D schematic and false-color scanning electron microscopy (SEM) image of a real FeS-FET device.[55] The influence of In_2Se_3 on the channel layer is also from its semiconducting property (see the schematic pictures in Figure 11A): the distribution of mobile charges depends on the position of the Fermi level relative to the conduction or the valence band. Due to a coupling of the ferroelectricity and semiconducting properties of In_2Se_3, the working mechanism of FeS-FET is more complicated than traditional FeFET. First, the drain current of the device is determined by both the top and the bottom surfaces due to the accumulation of charges. Second, the ferroelectric switching in this device is not only controlled by gate voltage, but also influenced by the movable carriers via the Coulomb screening effect. In turn, the movable charges are also influenced by the polarization state of In_2Se_3. Moreover, the strength of the electric field across the channel is considerably affected by the thickness and dielectric constant of the insulating layer. When the oxide thickness is large or dielectric constant is low, only local polarization can be achieved in the area near the channel/insulator interface. In the case of 90 nm thick SiO_2 as the insulating layer, the ON/OFF switching is accompanied by a unique clockwise hysteretic curve (Figure 11C,D). In contrast, when the oxide thickness is relatively small or dielectric constant is high, the electric field can easily pass through the In_2Se_3 channel and the top surface becomes conductive. Then, when the thinner 15 nm thick HfO_2 is used as the insulating layer, a counterclockwise hysteretic curve is observed (Figure 11E,F). The performance of the devices under different insulating layer thicknesses are summarized as follows. Within a high oxide thickness (90 nm SiO_2), the device exhibits a maximum drain current of 671 μA μm^{-1} at a supply gate voltage of 40 V. However, in the case of low oxide thickness (15 nm HfO_2), the device achieves a maximum drain current of 862 μA μm^{-1} at a lower supply gate voltage of 5 V and a more than 10^8 on/off ratio, which makes it applicable to low power consumption nonvolatile data memory.[55]

5.3 | Ferroelectric semiconductor junction/ferroelectric memristor

Similarly, using the semiconductor properties of 2D α In_2Se_3 ferroelectric, Si et al. also fabricated FSJ devices with a metal electrode-ferroelectric semiconductor–metal electrode structure.[57] Taking the advantage of the dipole coupling of In_2Se_3, the authors designed two FSJ devices that rely on the IP and OOP polarization of 2D α In_2Se_3, respectively. Figure 12A (left) shows the top-view schematic of a planar FST (p-FSJ). The electrodes are located on the left and right sides of the ferroelectric layer. The working mechanism of p-FSJ is somewhat similar to that of FeS-FET discussed in Section 5.2: the electrodes of p-FSJ correspond to the source and drain of FeS-FET.[55] However, for the crossbar FST (c-FSJ), the ferroelectric layer is vertically sandwiched between the top and bottom electrodes (as shown in Figure 12A, right). The false-color SEM images of p-FSJ and c-FSJ are shown in Figure 12B. The working mechanisms of the two FSJs are different. For the p-FSJ, the two electrodes (source and drain of FeS-FET) control the IP polarization and the gate controls the OOP polarization of the ferroelectric layer (see Figure 12C). As for the c-FSJ, the top-to-bottom voltage controls the OOP polarization of 2D α In_2Se_3 (shown in Figure 12D).[57] Figure 12E shows the I_D–V_{DS} curve of p-FSJ with 57.5 nm thick α In_2Se_3, and the channel length is 1 μm. As we can see, the on/off ratio increases with the increase of V_{GS} absolute value. When $V_{GS} = -4$ V, the

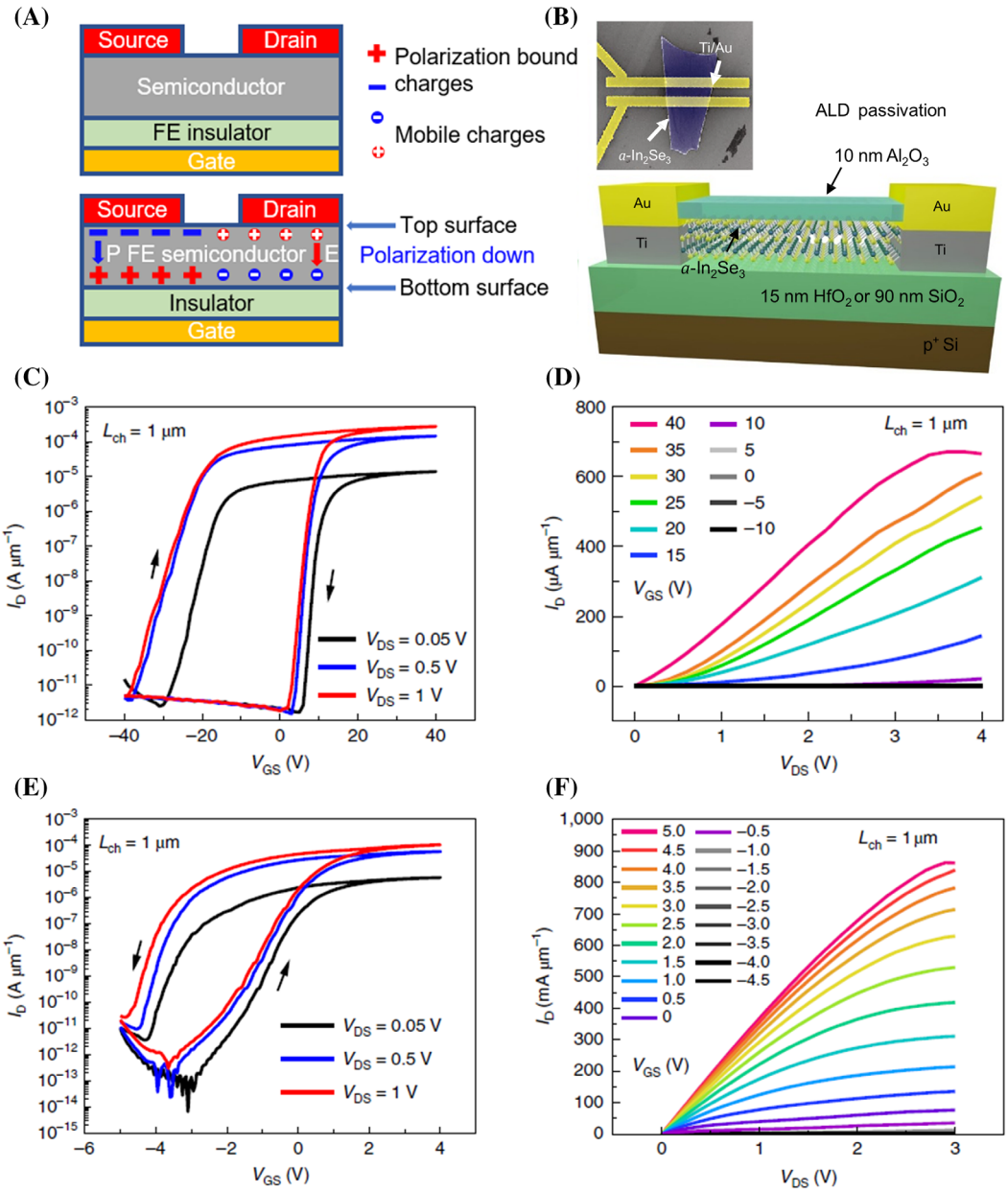

FIGURE 11 Structural and electrical measurements of 2D ferroelectric semiconductor channel field-effect transistors (FeS-FETs) device. (A) Schematics of FeFET (up) and FeS-FET (down), the blue and red arrows are the directions of the spontaneous polarization and the built-in electric field. (B) False-color image and 3D schematic of the 2D α In_2Se_3 FeS-FET. (C,D) I_D–V_{GS} and I_D–V_{DS} measurements of FeS-FET with 90 nm SiO_2 as the gate insulator. The length and thickness of the α In_2Se_3 channel are 1 μm and 52.2 nm, respectively. (E,F) I_D–V_{GS} and I_D–V_{DS} measurements of FeS-FET with 15 nm thick HfO_2 as the gate insulator. The length and thickness of the α In_2Se_3 channel are 1 μm and 92.1 nm, respectively. Reproduced with permission.[55] Copyright 2019, Springer Nature

on/off ratio reaches the maximum of 10^3. The *I*–*V* curve in Figure 12F shows the stable ferroelectric resistive switching of the c-FSJ with a 120 nm thick α In_2Se_3 within the ±2.5 V voltage range. Furthermore, c-FSJ has also shown its potential in the field of the synaptic device. The potentiation and depression profiles in Figure 12G were obtained using +2 and −2 V voltage, respectively. The pulse width ranges from 80 to 150 ns. Compared with the traditional synaptic devices, the c-FSJ exhibits great on-line learning accuracy of about 92%, low latency of 80 ns (for short write pulse width), and a large R_{ON} of 390 MΩ (for low energy consumption).[57]

In 2021, another asymmetric "metal-α In_2Se_3-Si" c-FSJ was proposed and experimentally confirmed to have the potential for low-power, high-density RRAM.[117] The bottom electrode of this asymmetric c-FSJ is heavily p^+ doped Si, and Ni was served as the top electrode. Compare with the symmetric "metal-α In_2Se_3-metal"

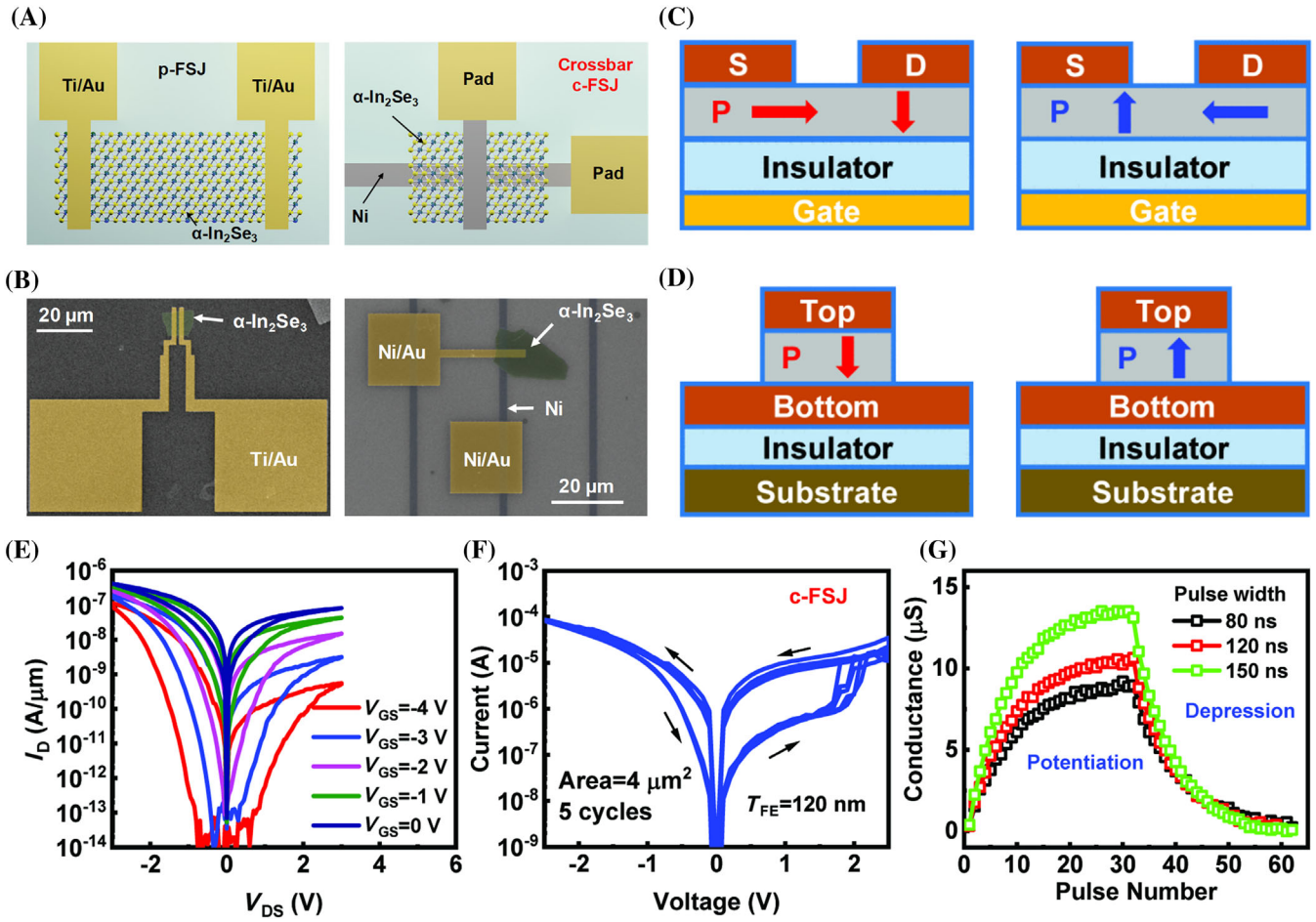

FIGURE 12 Structural and electrical measurements of ferroelectric semiconductor junction (FSJ) devices. (A) Schematics of the (left) planar FSJ (p-FSJ) and the (right) crossbar FSJ (c-FSJ). (B) Corresponding false-color image of p-FSJ (left) and c-FSJ (right) in (A). (C,D) Different directions of polarizations controlled by source-to-drain voltage (i.e., p-FSJ) and top-to-bottom electrode (i.e., c-FSJ). (E) I_D–V_{DS} curve of the p-FSJ with 57.5 nm thick α-In_2Se_3, the channel length is 1 μm. (F) *I–V* curve of the c-FSJ device with 120 nm thick α-In_2Se_3. (G) Potentiation and depression profile of c-FSJ with the voltage pulse width of 80–150 ns. +2 V and −2 V spikes are used for potentiation and depression, respectively. Reproduced with permission.[57] Copyright 2019, IEEE

c-FSJ, the depletion region in the p^+ Si electrode can modulate the height of the Schottky barrier through the polarization of the middle In_2Se_3. Through *I–V* characteristics, the asymmetric c-FSJ exhibits a high on/off ratio of 10^4 at 0.2 V, which is significantly higher than that of the symmetric c-FSJ.[57,117] In addition, α In_2Se_3-based asymmetric c-FSJ has a strong ability of high-temperature resistance. Experiments show that the asymmetric c-FSJ still has an on/off ratio of 10^3 at 140°C, demonstrating its application potential in extreme environments.[117]

In 2021, Gabel and Gu designed a planar memristor based on α In_2Se_3 p-FSJ and explored its resistance switching mechanism using PFM and Kelvin probe force microscopy (KPFM).[99] The top and bottom electrodes of this planar memristor are In (work function ≈ 4.09 eV) and Au (work function ≈ 5.4 eV), respectively (see Figure 13A). Thus, n-type α In_2Se_3 forms an ohmic contact with the top In electrode and a Schottky contact with the bottom Au electrode. With the top electrode biased and the bottom electrode grounded, the devices exhibit two types of *I–V* characteristics, that is, rectifying (Figure 13B) and symmetric (Figure 13C), which depends on the height of the Schottky barrier. For the rectifying device, the *I–V* relation hardly changes with the switching between high and low resistance states under forward voltage, which also shows that the inversion of polarization has little effect on the height of the Schottky barrier. Further, through PFM and KPFM, the authors directly probed the microscopic configuration of the domains and the surface potential of the α In_2Se_3 channel and ferroelectric-electrode interface. As shown in Figure 13D,E, at a low resistance state, the whole device exhibits a uniform

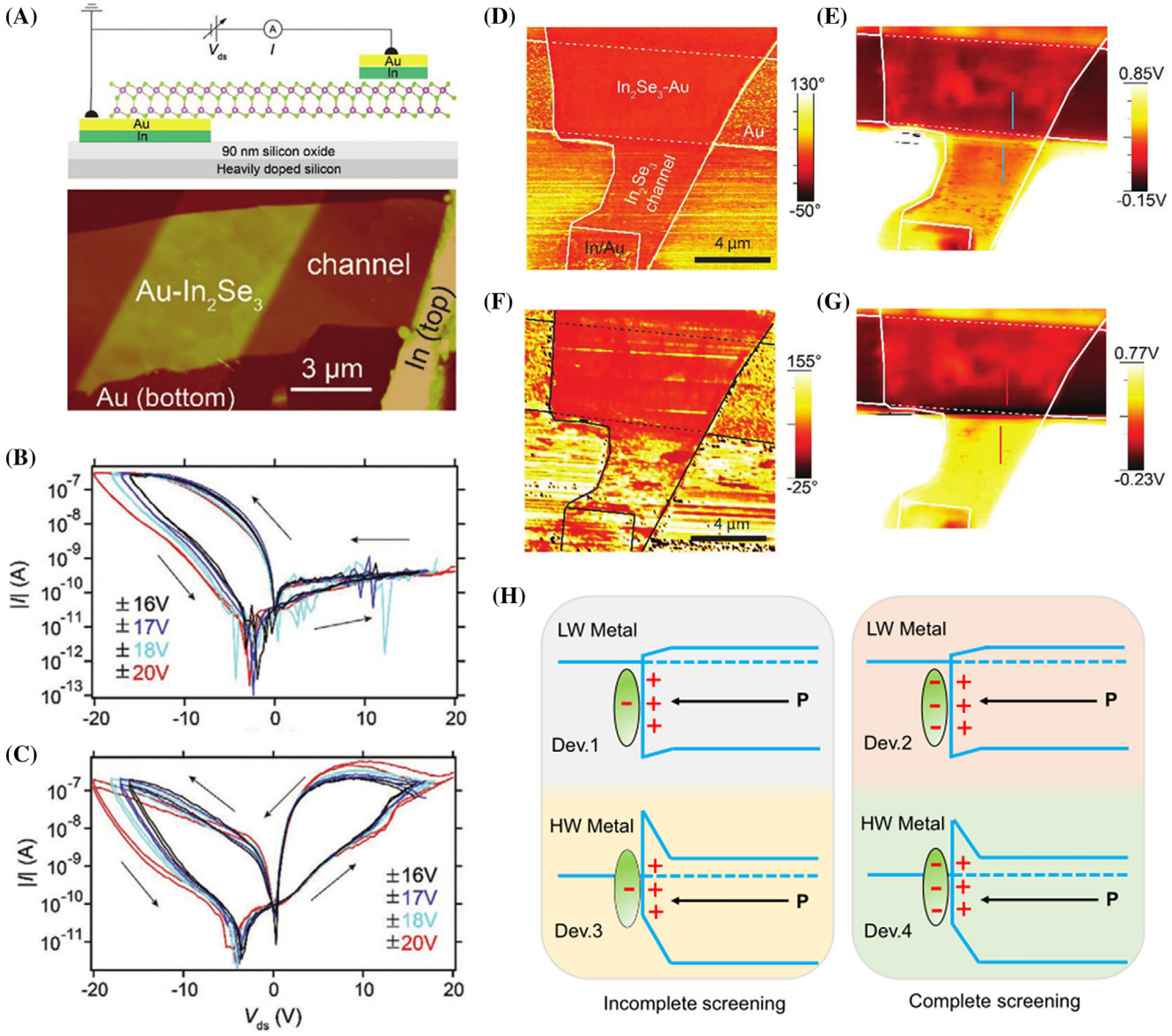

FIGURE 13 Characterization of resistance switching in ferroelectric memristors based on p-FSJs. (A) Schematic diagram and AFM image of a planar α In_2Se_3 based memristor. (B,C) *I–V* curves with rectified and symmetrical properties. OOP PFM phase and contact potential difference mapping of a rectifying device in (D,E) low resistance state and (F,G) high resistance state. Reproduced with permission.[99] Copyright 2021, John Wiley and Sons. (H) Band diagrams of four different p-FSJ devices in another research. The two devices on the left represent incomplete screening, while the two on the right represent complete screening. The top two devices indicate that low work function (LW) metals will be used as the electrode, while the bottom devices indicate that high work function (HW) metals will be employed. Reproduced with permission.[96] Copyright 2021, Springer Nature

polarization direction, but the potential of the α In_2Se_3–Au interface is lower than that of the channel. The difference in electric potential suggests a Schottky barrier between α In_2Se_3 and Au, which is consistent with the rectified *I–V* relationship in Figure 13B. When it comes to a high resistance state, domains with different polarization directions appear due to the inversion of polarization at the channel region. At the same time, the potential of the channel increases, while the potential of the α In_2Se_3-Au interface remains unchanged. The consistent PFM phase and electric potential at the interface in high and low resistance states suggest that the principle of resistance switching in this planar memristor is not the inversion of polarization at the metal-ferroelectric interface. However, the authors suggest that the change in band offset between the ferroelectric-electrode interface and the ferroelectric

channel caused by the ferroelectric switching may be responsible for the ferroelectric resistance switching.[99] The next year, Xue et al. explored the resistance switching mechanism of p-FSJ-based ferroelectric memristors through an interfacial engineering approach.[96] To verify the effect of ferroelectric polarization and interface barrier on ferroelectric resistance switching, the authors fabricated four devices, and the corresponding band diagrams are shown in Figure 13H. These devices differ in the work function height of the metal electrodes and the degree of interfacial screening of the ferroelectric polarization charges. Through electrical and PFM measurements, the authors found that ferroelectric resistance switching is affected together by ferroelectric polarization, variation of the Schottky barrier during operation, and the initial Schottky barrier height.[96]

5.4 | Ferroelectric channel transistors integrating ultrafast memory and neural computing

Although ferroelectric switching only involves two polarization states, analog signals beyond binary 0/1 can still be recorded by controlling the volume of polarization domains. Therefore, neuromorphic computing can be also realized in ferroelectric devices to overcome the von Neumann bottleneck.[118] In 2021, Wang et al. fabricated a

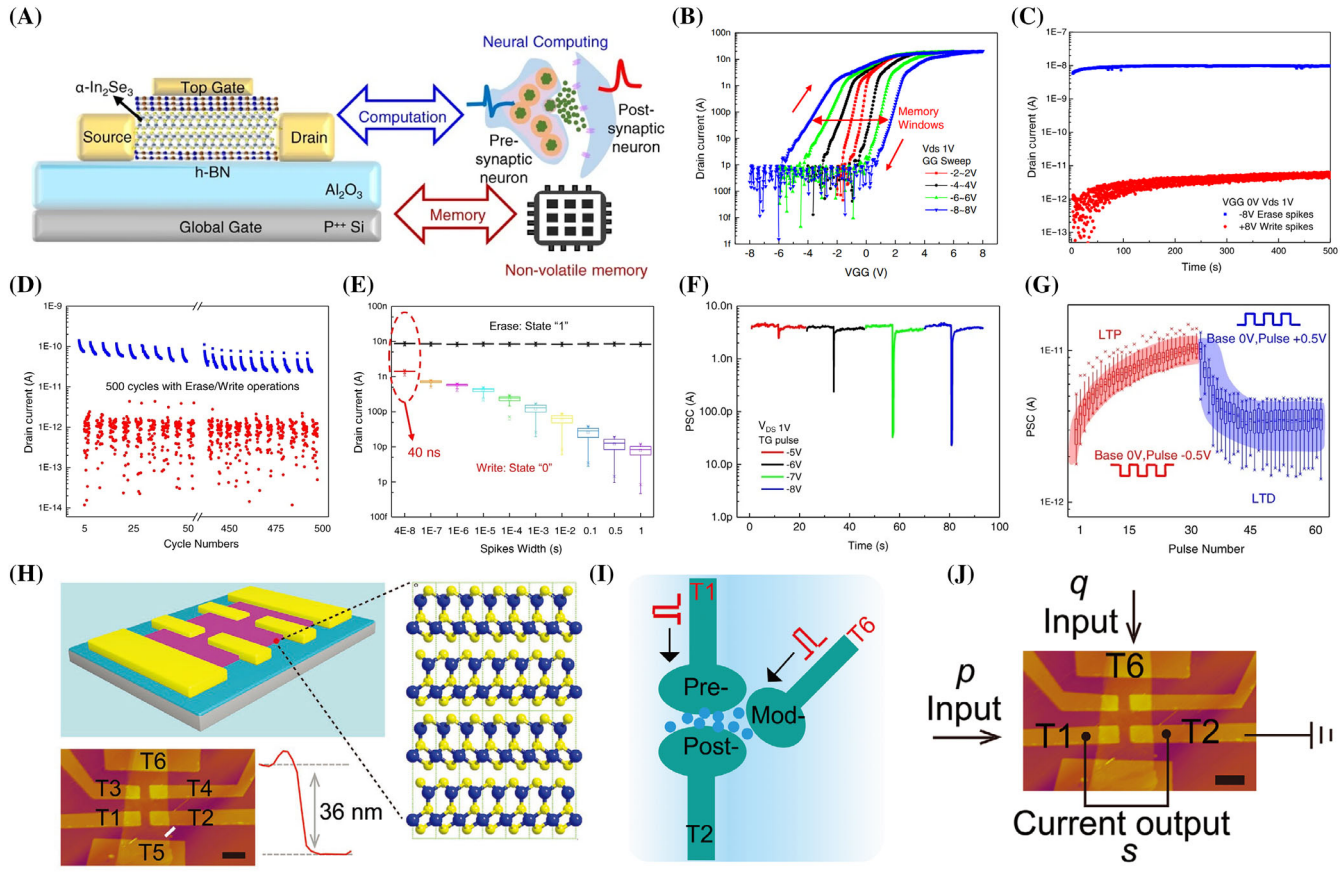

FIGURE 14 Structural and performance characterizations of 2D ferroelectric semiconductor channel field-effect transistors (FeCTs). (A) Schematic of 2D α In_2Se_3 FeCT, the neural computing function is controlled by the top gate and the nonvolatile memory function is realized by the global gate. (B) Transfer curves of 2D α In_2Se_3 FeCT under different global voltages, a maximum memory window of 6 V is achieved within −8 to 8 V scan voltage. (C) Retention performance measurement of 2D α In_2Se_3 FeCT, the on/off ratio is maintained over 10^3 within 500 s. (D) The endurance performance measurement of 2D α In_2Se_3 FeCT under 500 erasing and writing operations. (E) The programming speed of 2D α In_2Se_3 FeCT, a maximum speed of 40 ns is achieved with an on/off ratio of 10. (F) Transient response of ferroelectric channel current to spikes, showing short-term plasticity of 2D α In_2Se_3 FeCT. (G) The realization of progressive excitability and inhibition through ultra-low voltages, corresponding to long-term potentiation and long-term depression. Reproduced with permission.[56] Copyright 2021, Springer Nature. (H) Schematic, AFM topography image, and the atomic structure of α-In_2Se_3 ferroelectric memristor (scale bar, 2 μm). (I) Schematic of the operation of heterosynaptic plasticity. T1 and T2 are presynaptic and postsynaptic neurons, with the T6 terminal serving as a modulatory interneuron. (J) Schematic of the logic variables *p*, *q*, and output *s* in the device (scale bar, 2 μm). Reproduced with permission.[119] Copyright 2021, John Wiley and Sons

TABLE 2 Some representative progresses of 2D In_2Se_3 in the past 10 years

Year	Main affiliation	Finding	Technique	Method
2013	Washington State University, USA	Discovery of crystalline-crystalline phase transition in 2D In_2Se_3[67]	Electron microscopy, Raman spectra, and electrical measurements	Mechanical exfoliation
2013	Peking University, China	Controlled growth of atomically thin In_2Se_3 flakes[69]	Electron microscopy, AFM, and *I–V* characteristic	van der Waals epitaxy
2014	State University of New York, USA	High response to visible light[68]	Photocurrent measurements	Mechanical exfoliation
2015	Lorraine University, France	Discovery of dynamically stability of 2D In_2Se_3[63]	DFT	Atomic modeling
2015	Nanyang Technological University, Singapore	Controlled synthesis of high-quality 2D α In_2Se_3[134]	Raman/PL spectra, TEM, and photocurrent measurements	Physical vapor deposition
2015	Delft University of Technology, The Netherlands	Gate controlled photocurrent high-gain phototransistors based on 2D In_2Se_3[135]	AFM and optoelectronic measurements	Mechanical exfoliation
2017	University of Science and Technology of China, China	Prediction of intrinsic 2D ferroelectrics in In_2Se_3[45]	DFT	Atomic modeling
2017	Peking University, China	Proof of OOP piezoelectricity and ferroelectricity of layered 2D α-In_2Se_3 nanoflakes[46]	AFM, PFM, and *I–V* measurements	van der Waals epitaxy
2018	King Abdullah University of Science and Technology, Saudi Arabia	Observations of IP and OOP ferroelectricity in 2D α-In_2Se_3 at room temperature[49]	PFM, electrical measurements, and DFT	Chemical vapor deposition
2018	King Abdullah University of Science and Technology, Saudi Arabia	Coexistence of IP and OOP piezoelectricity in the monolayer to bulk α-In_2Se_3[51]	PFM, SHG, and piezoelectric current measurements	Mechanical exfoliation
2018	University of California, USA	Discovery of the dipole locking mechanism between IP and OOP polarization[50]	PFM and SHG	Mechanical exfoliation, and van der Waals epitaxy
2018	University of Science and Technology of China, China	Demonstration of switchable room-temperature ferroelectric diode based on 2D α-In_2Se_3[47]	PFM and *I–V* characteristic	Mechanical exfoliation
2018	Chongqing University, China	Observations of IP ferroelectricity in β′-In_2Se_3[52]	LEEM, PFM, STM, and DFT	Mechanical exfoliated
2019	University of Science and Technology of China, China	Demonstration of nonvolatile memory effect in 2D In_2Se_3 FeFET[54]	Electric measurements	Chemical vapor deposition
2019	Purdue University, USA	Fabrication of FeS-FET with 2D α-In_2Se_3 as the channel material[55]	*I–V* characteristics and PFM	Mechanical exfoliation
2019	Purdue University, USA	Scalable energy-efficient synaptic crossbar FSJ[57]	PFM and electrical measurements	Chemical vapor transport
2019	King Abdullah University of Science and Technology, Saudi Arabia	Demonstration of planar and vertical ferroelectric memristors with α-In_2Se_3[84]	PFM and electrical measurements	Mechanical exfoliation

(Continues)

TABLE 2 (Continued)

Year	Main affiliation	Finding	Technique	Method
2020	King Abdullah University of Science and Technology, Saudi Arabia	Demonstration of nonvolatile optical engineered ferroelectric domain wall[59]	PFM and electrical characterizations	Mechanical exfoliation
2021	Washington State University, USA	Understanding microscopic operating mechanisms of α-In_2Se_3 ferroelectric memristor[99]	PFM and KPFM	Mechanical exfoliation
2021	Fudan University, China	Proof of nonvolatile memory and neural computation functions of 2D α-In_2Se_3 FeCT[56]	PFM and electrical measurements	Mechanical exfoliation
2021	Jilin University, China	Discovery of the Mexican-hat PES and a new pseudo-centrosymmetric phase of 2D In_2Se_3[72]	DFT	Atomic modeling
2021	Zhejiang University, China	Unraveling the origin of ferroelectric resistance switching of α-In_2Se_3 memristor[96]	Electrical measurements, AFM, and PFM	Mechanical exfoliation

Abbreviations: AFM, atomic force microscopy; DFT, density-functional theory; FeCT, ferroelectric channel field-effect transistor; FeFET, ferroelectric field-effect transistor; FeS-FET, ferroelectric semiconductor channel field-effect transistor; FSJ, ferroelectric semiconductor junction; IP, in-plane; KPFM, Kelvin probe force microscopy; LEEM, low-energy electron microscopy; OOP, out-of-plane; PFM, piezoelectric force microscopy; SHG, second-harmonic generation; STM, scanning tunneling microscopy; TEM, transmission electron microscopy.

ferroelectric channel field-effect transistors (FeCT) device based on In_2Se_3, which integrates both neural computing and nonvolatile memory functions.[56] As shown in the schematic in Figure 14A, the global gate was heavily p-doped Si and the top gate dielectric layer was *h*-BN. A 30 nm thick Al_2O_3 grown by ALD was act as the global dielectric layer, the bottom *h*-BN layer prepared by mechanical exfoliation was used to optimize the interface and 40 nm thick α In_2Se_3 was employed as the channel layer.[56] The memory function is controlled by the global gate, and the working mechanism is the same as the FeS-FET discussed in Section 5.2.[55] The working mechanism of the top gate is similar to that of the global gate. However, due to the small area of the top gate, the top electric field cannot completely cover the channel, resulting in weaker polarization of the ferroelectric channel, which will depolarize to the initial state in a short time. When the pulse accumulates, the ferroelectric polarization of the channel is strengthened, and nonvolatile polarization is realized finally.[56] The coexisting volatility and non-volatility controlled by the top gate in 2D In_2Se_3 FeCTs are similar to the short-term and long-term plasticity of biology that neural computing expects to simulate.[118,120]

Figure 14B shows the transfer curves of 2D In_2Se_3 FeCT under a global gate voltage ranging from ±2 to ±8 V, and the source-drain voltage was 1 V. It can be seen that the transfer curves exhibit a clockwise hysteresis shape and the hysteresis memory window increases as the scan voltage range increases. A maximum memory window of 6 V under the sweeping voltage of −8 to +8 V is achieved. The device shows a rewritable nonvolatile signal contrast of more than three orders of magnitude and an endurance of over 500 erase and write cycles (see Figure 14C,D). When the pulse width for spiking ranges from 1 s to 40 ns, the drain current varies from ~10 pA to ~1 nA (see Figure 14E).[56] The gradually changed drain current may be a resultant effect of partial switching of polarization and carrier drifting under electric fields. Ultrafast time-resolved detection of polarization state may be helpful to further clarify their roles.

Finally, to realize the function of neural computing, the top gate voltage and the corresponding channel current are regarded as the presynaptic input and post-synaptic current (PSC), respectively. As shown in Figure 14F, when a short spike was applied, the PSC exhibited a transient signal response and then quickly return to its initial state, which shows a kind of synaptic short-term plasticity. The long-term plasticity including the long-term potentiation and the long-term depression was also achieved by negative and positive voltage pulses, respectively (shown in Figure 14G). The calculated power consumption for excitation and inhibition are 234 and 40 fJ per event, which shows its great application potential in the field of low-power neuromorphic computing systems.[56] It is worth noting that the OFF current of such a FeCT is very sensitive to temperature. For example, when

temperature increases from 300 to 423 K, the OFF current increases more than 5 orders of magnitude.[56] The underlying reason may be thermally induced charge relaxations and structure transitions. On one hand, this phenomenon may influence the reliability of the device. But on the other hand, it also provides a new degree to control the device.[56]

The works above pioneered the realization of In_2Se_3-based FeCT that integrates memory and computing functions. Compared with traditional FeFET memories, the write speed has greatly improved to 40 ns. The on/off ratio depends on the voltage pulse width. When the pulse width increases from 40 ns to 1 s, the on/off ratio increases from 10 to 10^3. In addition, the FeCT also integrates computing functional with a low energy consumption of 234/40 fJ per spike for excitation/inhibition.[56]

Besides, In_2Se_3 can also be used in heterosynaptic devices to realize neuromorphic in-memory computing functions. In 2021, Xue et al. realized a heterosynaptic memristor with an on/off ratio greater than 10^3 and successfully achieved heterosynaptic plasticity (Figure 14H–J).[119] Unlike similar volatile devices, the memristor device in this work is nonvolatile and experiments show that the high switching ratio can last up to 2 days.[121] Furthermore, the nonvolatile control of the channel current by the third terminal of the α-In_2Se_3 memristor enables the device to have the ability to simulate associative heterosynaptic learning with ultralow read energy of picojoule (see Figure 14I). Additionally, using three of the six terminals, Boolean logic can also be implemented in the heterosynaptic devices with ultralow picoampere operating currents. This work shows that In_2Se_3 ferroelectric devices have great application potential in neuromorphic and in-memory computing, and is expected to break through the von Neumann bottleneck.[119]

5.5 | Crystal growth of 2D In_2Se_3

In order to realize practical applications of ferroelectric data storage and computation, the growth of high-quality 2D In_2Se_3 is necessary. Although bulk In_2Se_3 has been known for many years, the controllable and selective growth of large-scale 2D In_2Se_3 is still a great challenge due to the complex stoichiometric species and numerous phases in the indium selenide system.[87–89,122–124] In 2017, Almeida et al. succeeded in the low-temperature colloidal synthesis of β In_2Se_3 nanosheets with tunable lateral dimensions ranging from 300 to 900 nm and a thickness of monolayer, short amino nitriles (dicyandiamide or cyanamide) was used as shape-controlling agents.[125] In 2018, through physical vapor transport, Balakrishnan et al. grew a large-area ($>10^3$ μm^2) β In_2Se_3 film with the thinnest thickness of 4 nm on the surface of ε-GaSe crystals.[126] Due to the natural van der Waals layered structure of β In_2Se_3, the mechanical exfoliation method can also be used to prepare ultrathin films.[52,127] According to previous studies, β In_2Se_3 with a thickness of 7–760 nm has been successfully exfoliated.[52,127] Besides, CVD and MBE methods are also used to fabricate β In_2Se_3 with thicknesses ranging from a single layer to tens of layers.[66,73–76,128,129] In 2021, Rashid et al. successfully fabricated γ In_2Se_3 nanoflakes with thickness ranging from 13.6 to 90.5 nm by CVD method.[77]

The methods currently used to prepare few/monolayer α In_2Se_3 include CVD,[50] chemical vapor transport,[130] MBE,[58] mechanical exfoliation,[48,51] and van der Waals epitaxy.[67,69] In 2013, Lin et al. successfully synthesized α In_2Se_3 with thickness ranging from 1.3 to 3.3 nm, where the lateral dimension of the 1.3 nm thick region exceeded 100 μm.[69] In 2017, Zhou et al. prepared ultrathin α In_2Se_3 film with an area of several square microns and a thickness of 3–120 nm through the mechanical exfoliation method.[46] In 2018, through the CVD method, Xiao et al. synthesized α In_2Se_3 with a thickness of several nanometers and a lateral dimension of tens of micrometers.[50] At present, α In_2Se_3 with thickness ranging from several nanometers to hundreds of nanometers has been prepared successfully. The characterizations of the samples show that In_2Se_3 exhibits regular shapes and boundaries when the thickness is ≥2 nm, indicating good crystallinity, while when the thickness decreases below 1.3 nm, it exhibits irregular shapes.[49] Limited by the trade-off between thickness and crystal quality, the thickness of the In_2Se_3 in the current reported devices is mainly tens of nanometers.[54–57,96,117,119] Therefore, it is urgent to seek a method for mass-produce high-quality 2D In_2Se_3 toward industrial applications.

6 | CONCLUSION AND OUTLOOK

2D In_2Se_3 has become a research hotspot in the field of ferroelectrics due to its stable ferroelectricity at room temperature. The robust ferroelectricity of 2D In_2Se_3 origins from its asymmetric configuration and bonding type, which is in contrast to the slight offset of the central atoms in traditional displacement-type ferroelectrics. As such, both the elimination of ferroelectricity and the ferroelectric switching of 2D In_2Se_3 are considered to be accompanied by the breaking and formation of chemical bonds. This re-bonding mechanism enables 2D In_2Se_3 to resist depolarization fields even at its monolayer thickness limit. The ferroelectric transition of 2D In_2Se_3 can also be regarded as the order-to-order phase transition. Therefore, the name "phase-change-type ferroelectrics" should be more suitable to express the essential characteristics of this kind of 2D ferroelectric material.

Here, we also try to summarize the structural and electronic characteristics of the phase-change-type ferroelectrics to inspire or search for new robust 2D ferroelectric materials. (1) Van der Waals layered materials should be considered to ensure that stable 2D or quasi-2D counterparts can be fabricated. (2) The break of inverse symmetry in a monolayer is needed to provide ferroelectricity. (3) A relatively flexible chemical bonding, such as the competing covalent-ionic bonding or metavalent bonding[131] or hyperbonding[132] or resonant bonding,[133] may be the key to enabling fast polarization switching.

Next, Table 2 lists some representative works of 2D In_2Se_3 in the past 10 years. At the early stage, 2D In_2Se_3 was considered to be a promising candidate for phase-change memory due to the observation of its crystalline-to-crystalline phase transition.[67] Since 2017, the year when 2D In_2Se_3 was predicted to be ferroelectric,[45] the ferroelectricity of 2D α In_2Se_3 has been continuously verified by experiments.[46,47,49,50] Further, more and more ferroelectric memories and computing devices based on In_2Se_3 have been successfully demonstrated,[54–57,60] as discussed in this work.

However, as an emerging ferroelectric material, the study on 2D In_2Se_3 is still in its early stage. In-depth research is still needed to further improve the performance in practical applications. Here, we summarize crucial problems or challenges in this field and try to give suggestions for possible solutions and new prospects: (1) 2D In_2Se_3 has several different crystalline phases that are involved in ferroelectric switching. The atomic picture and the full dynamic processes of reversible switching are still not fully understood. The combination of first-principles calculations and experiments may provide valuable information at the atomic scale. Further, controlling the evolution of domain walls during ferroelectric switching is a key issue to improve device performance. Therefore, some new techniques such as machine-learning atomic potential simulation could be an option to study the problem. (2) Although In_2Se_3 can maintain stable ferroelectricity even at the monolayer limit by the re-bonding mechanism, this mechanism and the entropy barrier caused by the paraelectric phase also affect the speed of its ferroelectric polarization switching.[72] For example, the switching time of $BaTiO_3$ can reach 200 ps,[103] while the experimentally reported switching time of 2D In_2Se_3 is at the scale from tens of nanoseconds to even microseconds.[54,56] Of course, the read and write speed of the actual device is also affected by geometries and measurement tools. Therefore, performance such as speed, retention, reliability, and endurance still need to be systematically investigated and further improved. (3) The memory/computing devices based on FeCT, where 2D In_2Se_3 also serves as the channel, show interesting features and promising performance. However, the underlying mechanism of the device is complicated, which is possibly related to ferroelectric switching, phase transition, carrier relaxation, and IP ferroelectricity. The clarification of these issues is necessary for device optimizations. (4) Because the IP ferroelectricity of 2D α In_2Se_3 is much stronger than the OOP ferroelectricity, developing the application of the IP ferroelectricity should be a valuable subject, like FeCT or FeS-FET mentioned before. (5) Although 2D and quasi-2D In_2Se_3 films have been fabricated, a mature method to grow large-scale and high-quality 2D In_2Se_3 films with a low cost is urgently required to meet the demands of industrial applications. (6) Note that currently reported devices are based on quasi-2D In_2Se_3 films with a thickness of tens of nanometers. The demonstration of ferroelectric devices based on single-layer or few-layer In_2Se_3 is very much anticipated. Meanwhile, it is an open question whether the physics of monolayer In_2Se_3 is still the same as the one learned from quasi-2D samples. (7) According to the origin of the robust ferroelectricity of 2D In_2Se_3 known from its phase-transition mechanism and the special bonding type, high-throughput calculations can be employed to find or design more 2D ferroelectric materials in the future. We sincerely hope this review could draw the attention of the experts in the scientific community and help accelerate the industrial applications for this rising ferroelectric information material.

ACKNOWLEDGMENTS

Work in China was supported by the National Natural Science Foundation of China (Grants Nos. 61922035, 11904118, and 11874171), the Fundamental Research Funds for the Central Universities, and China Postdoctoral Science Foundation (2019 M661200).

CONFLICT OF INTEREST

The authors declare no conflict of interest.

ORCID

Xian-Bin Li https://orcid.org/0000-0002-0046-2016

REFERENCES

1. Cai FX, Correll JM, Lee SH, et al. A fully integrated reprogrammable memristor-CMOS system for efficient multiply-accumulate operations. *Nat Electron*. 2019;2(7):290-299.
2. Li C, Hu M, Li YN, et al. Analogue signal and image processing with large memristor crossbars. *Nat Electron*. 2018;1(1):52-59.
3. Hwang CS. Prospective of semiconductor memory devices: from memory system to materials. *Adv Electron Mater*. 2015;1(6):1400056.

4. Editorial. Big data needs a hardware revolution. *Nature*. 2018; 2018(554):145-146.
5. Zhang Z, Wang Z, Shi T, et al. Memory materials and devices: from concept to application. *InfoMat*. 2020;2(2):261-290.
6. Semiconductor Industry Association. International Technology Roadmap for Semiconductors (ITRS). 2015. Accessed Jun 05, 2015. https://www.semiconductors.org/resources/2015-international-technology-roadmap-for-semiconductors-itrs/.
7. Scott JF, Paz de Araujo CA. Ferroelectric memories. *Science*. 1989;246(4936):1400-1405.
8. Scott JF. Applications of modern ferroelectrics. *Science*. 2007; 315(5814):954-959.
9. Martin LW, Rappe AM. Thin-film ferroelectric materials and their applications. *Nat Rev Mater*. 2017;2(2):14.
10. Buck DA. *Ferroelectrics for Digital Information Storage and Switching*. Massachusetts Institute of Tech Cambridge Digital Computer Lab; 1952.
11. Boyn S, Girod S, Garcia V, et al. High-performance ferroelectric memory based on fully patterned tunnel junctions. *Appl Phys Lett*. 2014;104(5):052909.
12. Kim RH, Kim HJ, Bae I, et al. Non-volatile organic memory with sub-millimetre bending radius. *Nat Commun*. 2014;5(1): 3583.
13. Jang S, Jang S, Lee E-H, Kang M, Wang G, Kim T-W. Ultrathin conformable organic artificial synapse for wearable intelligent device applications. *ACS Appl Mater Interfaces*. 2019;11(1):1071-1080.
14. Lee YR, Trung TQ, Hwang B-U, Lee N-E. A flexible artificial intrinsic-synaptic tactile sensory organ. *Nat Commun*. 2020; 11(1):2753.
15. Ahn CH, Rabe KM, Triscone JM. Ferroelectricity at the nanoscale: local polarization in oxide thin films and heterostructures. *Science*. 2004;303(5657):488-491.
16. Bondurant DW, Gnadinger FP. Ferroelectrics for nonvolatile RAMs. *IEEE Spectr*. 1989;26(7):30-33.
17. Evans JT, Womack R. An experimental 512-bit nonvolatile memory with ferroelectric storage cell. *IEEE J Solid-State Circuit*. 1988;23(5):1171-1175.
18. Sinharoy S, Buhay H, Lampe DR, Francombe MH. Integration of ferroelectric thin films into nonvolatile memories. *J Vac Sci Technol A*. 1992;10(4):1554-1561.
19. Kim K. Technology perspective for 1T/1C fram. *Integr Ferroelectr*. 1999;25(1–4):149-167.
20. Scott JF. Nano-ferroelectrics. In: Tsakalakos T, Ovid'ko IA, Vasudevan AK, eds. *Nanostructures: Synthesis, Functional Properties and Applications*. Springer Science & Business Media; 2003:583-600.
21. Mitra S, Humes J. An optimized package test methodology for testing FRAM((R)) memories. *Integr Ferroelectr*. 1999;26(1–4): 999-1012.
22. Lee S-S, Noh K-H, Kang H-B, Hong S-K, Yeom S-J, Park Y-J. Characterization of Hynix 16M feram adopted novel sensing scheme. *Integr Ferroelectr*. 2003;53(1):343-351.
23. Schaller RR. Moore's law: past, present and future. *IEEE Spectr*. 1997;34(6):52-59.
24. Liu C, Chen H, Wang S, et al. Two-dimensional materials for next-generation computing technologies. *Nat Nanotechnol*. 2020;15(7):545-557.
25. Liu L, Liu C, Jiang L, et al. Ultrafast non-volatile flash memory based on van der Waals heterostructures. *Nat Nanotechnol*. 2021;16(8):874-881.
26. Wang X-P, Li X-B, Chen N-K, Chen B, Rao F, Zhang S. Phase-change-memory process at the limit: a proposal for utilizing monolayer Sb_2Te_3. *Adv Sci*. 2021;8(13):2004185.
27. Mehta RR, Silverman BD, Jacobs JT. Depolarization fields in thin ferroelectric films. *J Appl Phys*. 1973;44(8):3379-3385.
28. Birol T. Stable and switchable polarization in 2D. *Nature*. 2018;560(7717):174-175.
29. Zhong WL, Wang YG, Zhang PL, Qu BD. Phenomenological study of the size effect on phase transitions in ferroelectric particles. *Phys Rev B*. 1994;50(2):698-703.
30. Junquera J, Ghosez P. Critical thickness for ferroelectricity in perovskite ultrathin films. *Nature*. 2003;422(6931):506-509.
31. Kim YS, Kim DH, Kim JD, et al. Critical thickness of ultrathin ferroelectric $BaTiO_3$ films. *Appl Phys Lett*. 2005; 86(10):102907.
32. Gerra G, Tagantsev AK, Setter N, Parlinski K. Ionic polarizability of conductive metal oxides and critical thickness for ferroelectricity in $BaTiO_3$. *Phys Rev Lett*. 2006;96(10):107603.
33. Tinte S, Stachiotti MG. Surface effects and ferroelectric phase transitions in $BaTiO_3$ films. *Phys Rev B*. 2001;64(23):235403.
34. Wu Z, Huang N, Liu Z, et al. Ferroelectricity in $Pb(Zr_{0.5}Ti_{0.5})O_3$ thin films: critical thickness and 180° stripe domains. *Phys Rev B*. 2004;70(10):104108.
35. Sepliarsky M, Stachiotti MG, Migoni RL. Interface effects in ferroelectric $PbTiO_3$ ultrathin films on a paraelectric substrate. *Phys Rev Lett*. 2006;96(13):137603.
36. Choi KJ, Biegalski M, Li YL, et al. Enhancement of ferroelectricity in strained $BaTiO_3$ thin films. *Science*. 2004;306(5698): 1005-1009.
37. Sai N, Kolpak AM, Rappe AM. Ferroelectricity in ultrathin perovskite films. *Phys Rev B*. 2005;72(2):020101.
38. Zhang Y, Li G-P, Shimada T, Wang J, Kitamura T. Disappearance of ferroelectric critical thickness in epitaxial ultrathin $BaZrO_3$ films. *Phys Rev B*. 2014;90(18):184107.
39. Cui C, Xue F, Hu W-J, Li L-J. Two-dimensional materials with piezoelectric and ferroelectric functionalities. *npj 2D Mater Appl Ther*. 2018;2(1):18.
40. Guan Z, Hu H, Shen XW, et al. Recent progress in two-dimensional ferroelectric materials. *Adv Electron Mater*. 2020; 6(1):1900818.
41. Xue F, He J-H, Zhang X. Emerging van der Waals ferroelectrics: unique properties and novel devices. *Appl Phys Rev*. 2021;8(2):021316.
42. Qi L, Ruan S, Zeng Y-J. Review on recent developments in 2D ferroelectrics: theories and applications. *Adv Mater*. 2021; 33(13):2005098.
43. Liu F, You L, Seyler KL, et al. Room-temperature ferroelectricity in $CuInP_2S_6$ ultrathin flakes. *Nat Commun*. 2016;7(1): 12357.
44. Chang K, Liu J, Lin H, et al. Discovery of robust in-plane ferroelectricity in atomic-thick SnTe. *Science*. 2016;353(6296): 274-278.
45. Ding W, Zhu J, Wang Z, et al. Prediction of intrinsic two-dimensional ferroelectrics in In_2Se_3 and other III_2-VI_3 van der Waals materials. *Nat Commun*. 2017;8:14956.

46. Zhou Y, Wu D, Zhu Y, et al. Out-of-plane piezoelectricity and ferroelectricity in layered alpha-In_2Se_3 nanoflakes. *Nano Lett*. 2017;17(9):5508-5513.
47. Wan S, Li Y, Li W, Mao X, Zhu W, Zeng H. Room-temperature ferroelectricity and a switchable diode effect in two-dimensional α-In_2Se_3 thin layers. *Nanoscale*. 2018;10(31):14885-14892.
48. Xue F, Hu W, Lee K-C, et al. Room-temperature ferroelectricity in hexagonally layered α-In_2Se_3 nanoflakes down to the monolayer limit. *Adv Funct Mater*. 2018;28(50):1803738.
49. Cui CJ, Hu WJ, Yan XG, et al. Intercorrelated in-plane and out-of-plane ferroelectricity in ultrathin two-dimensional layered semiconductor In_2Se_3. *Nano Lett*. 2018;18(2):1253-1258.
50. Xiao J, Zhu H, Wang Y, et al. Intrinsic two-dimensional ferroelectricity with dipole locking. *Phys Rev Lett*. 2018;120(22):227601.
51. Xue F, Zhang J, Hu W, et al. Multidirection piezoelectricity in mono- and multilayered hexagonal α-In_2Se_3. *ACS Nano*. 2018;12(5):4976-4983.
52. Zheng CX, Yu L, Zhu L, et al. Room temperature in-plane ferroelectricity in van der Waals In_2Se_3. *Sci Adv*. 2018;4(7):eaar7720.
53. Xu C, Chen Y, Cai X, et al. Two-dimensional antiferroelectricity in nanostripe-ordered In_2Se_3. *Phys Rev Lett*. 2020;125(4):047601.
54. Wan SY, Li Y, Li W, et al. Nonvolatile ferroelectric memory effect in ultrathin-In_2Se_3. *Adv Funct Mater*. 2019;29(20):1808606.
55. Si MW, Saha AK, Gao SJ, et al. A ferroelectric semiconductor field-effect transistor. *Nat Electron*. 2019;2(12):580-586.
56. Wang S, Liu L, Gan L, et al. Two-dimensional ferroelectric channel transistors integrating ultra-fast memory and neural computing. *Nat Commun*. 2021;12(1):53.
57. Si M, Luo Y, Chung W, et al. A novel scalable energy-efficient synaptic device: crossbar ferroelectric semiconductor junction. 2019 IEEE International Electron Devices Meeting (IEDM). IEEE; 2019; 130-133.
58. Poh SM, Tan SJR, Wang H, et al. Molecular-beam epitaxy of two-dimensional In_2Se_3 and its giant electroresistance switching in ferroresistive memory junction. *Nano Lett*. 2018;18(10):6340-6346.
59. Xue F, He X, Liu WH, et al. Optoelectronic ferroelectric domain-wall memories made from a single van der Waals ferroelectric. *Adv Funct Mater*. 2020;30(52):2004206.
60. Wang L, Wang X, Zhang Y, et al. Exploring ferroelectric switching in α-In_2Se_3 for neuromorphic computing. *Adv Funct Mater*. 2020;30(45):2004609.
61. Popović S, Čelustka B, Bidjin D. X-ray diffraction measurement of lattice parameters of In_2Se_3. *Phys Status Solidi A*. 1971;6(1):301-304.
62. Osamura K, Murakami Y, Tomiie Y. Crystal structures of α-and β-indium selenide, In_2Se_3. *J Physical Soc Japan*. 1966;21(9):1848.
63. Debbichi L, Eriksson O, Lebègue S. Two-dimensional indium selenides compounds: an ab initio study. *J Phys Chem Lett*. 2015;6(15):3098-3103.
64. Li Y, Gong M, Zeng HL. Atomically thin alpha-In_2Se_3: an emergent two-dimensional room temperature ferroelectric semiconductor. *J Semicond*. 2019;40(6):061002.
65. Küpers M, Konze PM, Meledin A, et al. Controlled crystal growth of indium selenide, In_2Se_3, and the crystal structures of α-In_2Se_3. *Inorg Chem*. 2018;57(18):11775-11781.
66. Liu L, Dong J, Huang J, et al. Atomically resolving polymorphs and crystal structures of In_2Se_3. *Chem Mater*. 2019;31(24):10143-10149.
67. Tao X, Gu Y. Crystalline–crystalline phase transformation in two-dimensional In_2Se_3 thin layers. *Nano Lett*. 2013;13(8):3501-3505.
68. Jacobs-Gedrim RB, Shanmugam M, Jain N, et al. Extraordinary photoresponse in two-dimensional In_2Se_3 nanosheets. *ACS Nano*. 2014;8(1):514-521.
69. Lin M, Wu D, Zhou Y, et al. Controlled growth of atomically thin In_2Se_3 flakes by van der Waals epitaxy. *J Am Chem Soc*. 2013;135(36):13274-13277.
70. Wu D, Pak AJ, Liu Y, et al. Thickness-dependent dielectric constant of few-layer In_2Se_3 Nanoflakes. *Nano Lett*. 2015;15(12):8136-8140.
71. Liu J, Pantelides ST. Pyroelectric response and temperature-induced α-β phase transitions in α-In_2Se_3 and other α-III_2VI_3 (III = Al, Ga, In; VI = S, Se) monolayers. *2D Mater*. 2019;6(2):025001.
72. Huang Y-T, Chen N-K, Li Z-Z, et al. Mexican-hat potential energy surface in two-dimensional III_2-VI_3 materials and the importance of entropy barrier in ultrafast reversible ferroelectric phase change. *Appl Phys Rev*. 2021;8(3):031413.
73. Zhang F, Wang Z, Dong J, et al. Atomic-scale observation of reversible thermally driven phase transformation in 2D In_2Se_3. *ACS Nano*. 2019;13(7):8004-8011.
74. Chen Z, Fu W, Wang L, et al. Atomic imaging of electrically switchable striped domains in β′-In_2Se_3. *Adv Sci*. 2021;8(17):2100713.
75. Zhang F, Wang Z, Liu L, et al. Atomic-scale visualization of polar domain boundaries in ferroelectric In_2Se_3 at the monolayer limit. *J Phys Chem Lett*. 2021;12(49):11902-11909.
76. Zhang Z, Nie J, Zhang Z, Yuan Y, Fu Y-S, Zhang W. Atomic visualization and switching of ferroelectric order in β-In_2Se_3 films at the single layer limit. *Adv Mater*. 2021;34(3):2106951.
77. Rashid R, Ling FC-C, Wang S-P, et al. IP and OOP ferroelectricity in hexagonal γ-In_2Se_3 nanoflakes grown by chemical vapor deposition. *J Alloys Compd*. 2021;870:159344.
78. Eerenstein W, Mathur ND, Scott JF. Multiferroic and magnetoelectric materials. *Nature*. 2006;442(7104):759-765.
79. Nan CW, Bichurin MI, Dong SX, Viehland D, Srinivasan G. Multiferroic magnetoelectric composites: historical perspective, status, and future directions. *J Appl Phys*. 2008;103(3):35.
80. Nguyen TD, Deshmukh N, Nagarah JM, et al. Piezoelectric nanoribbons for monitoring cellular deformations. *Nat Nanotechnol*. 2012;7(9):587-593.
81. Balke N, Bdikin I, Kalinin SV, Kholkin AL. Electromechanical imaging and spectroscopy of ferroelectric and piezoelectric materials: state of the art and prospects for the future. *J Am Ceram Soc*. 2009;92(8):1629-1647.
82. Lv B, Yan Z, Xue W, et al. Layer-dependent ferroelectricity in 2H-stacked few-layer α-In_2Se_3. *Mater Horiz*. 2021;8(5):1472-1480.
83. Klein MW, Enkrich C, Wegener M, Linden S. Second-harmonic generation from magnetic metamaterials. *Science*. 2006;313(5786):502-504.

84. Xue F, He X, Retamal JRD, et al. Gate-tunable and multidirection-switchable memristive phenomena in a van der Waals ferroelectric. *Adv Mater*. 2019;31(29):1901300.
85. Miyazawa H, Sugaike S. Phase transition of In_2Se_3. *J Physical Soc Japan*. 1957;12(3):312.
86. Newman PC. Phase changes in In_2Se_3. *Z Anorg Allg Chem*. 1959;299(3–4):158-159.
87. Van Landuyt J, Van Tendeloo G, Amelinckx S. Phase transitions in In_2Se_3 as studied by electron microscopy and electron diffraction. *Phys Status Solidi A*. 1975;30(1):299-314.
88. Ye J, Soeda S, Nakamura Y, Nittono O. Crystal structures and phase transformation in In_2Se_3 compound semiconductor. *Jpn J Appl Phys*. 1998;37, (Part 1), (8):4264-4271.
89. Popovic S, Tonejc A, Grzeta-Plenkovic B, Celustka B, Trojko R. Revised and new crystal data for indium selenides. *J Appl Cryst*. 1979;12(4):416-420.
90. Likforman A, Carre D, Hillel R. Structure cristalline du seleniure d'indium In_2Se_3. *Acta Crystallogr B*. 1978;34(1):1-5.
91. Likforman A, Fourcroy P-H, Guittard M, Flahaut J, Poirier R, Szydlo N. Transitions de la forme de haute température α de In_2Se_3, de part et d'autre de la température ambiante. *J Solid State Chem*. 1980;33(1):91-97.
92. Julien C, Eddrief M, Kambas K, Balkanski M. Electrical and optical properties of In_2Se_3 thin films. *Thin Solid Films*. 1986; 137(1):27-37.
93. Kim H-G, Min I-S, Kim W-T. Phase transition temperature of the α-In_2Se_3 single crystal. *Solid State Commun*. 1987;64(5): 819-822.
94. Manolikas C. New results on the phase transformations of In_2Se_3. *J Solid State Chem*. 1988;74(2):319-328.
95. Ding J, Shao D-F, Li M, Wen L-W, Tsymbal EY. Two-dimensional antiferroelectric tunnel junction. *Phys Rev Lett*. 2021;126(5):057601.
96. Xue F, He X, Ma Y, et al. Unraveling the origin of ferroelectric resistance switching through the interfacial engineering of layered ferroelectric-metal junctions. *Nat Commun*. 2021;12(1):7291.
97. Zhang Y, Wang L, Chen H, Ma T, Lu X, Loh KP. Analog and digital mode α-In_2Se_3 memristive devices for neuromorphic and memory applications. *Adv Electron Mater*. 2021;7(12): 2100609.
98. Ma TP, Jin-Ping H. Why is nonvolatile ferroelectric memory field-effect transistor still elusive? *IEEE Electron Device Lett*. 2002;23(7):386-388.
99. Gabel M, Gu Y. Understanding microscopic operating mechanisms of a van der Waals planar ferroelectric Memristor. *Adv Funct Mater*. 2021;31(9):2009999.
100. Muller J, Boscke TS, Schroder U, Hoffmann R, Mikolajick T, Frey L. Nanosecond polarization switching and long retention in a novel MFIS-FET based on ferroelectric HfO_2. *IEEE Electron Device Lett*. 2012;33(2):185-187.
101. Chung W, Si M, Shrestha PR, Campbell JP, Cheung KP, Ye PD. First direct experimental studies of $Hf_{0.5}Zr_{0.5}O_2$ ferroelectric polarization switching down to 100-picosecond in sub-60 mV/dec germanium ferroelectric nanowire FETs. 2018 IEEE Symposium on VLSI Technology. IEEE; 2018; 89-90.
102. Dünkel S, Trentzsch M, Richter R, et al. A FeFET based super-low-power ultra-fast embedded NVM technology for 22 nm FDSOI and beyond. 2017 IEEE International Electron Devices Meeting (IEDM). IEEE; 2017; 19.7.1-19.7.4.
103. Li J, Nagaraj B, Liang H, Cao W, Lee CH, Ramesh R. Ultrafast polarization switching in thin-film ferroelectrics. *Appl Phys Lett*. 2004;84(7):1174-1176.
104. Larsen PK, Kampschöer GLM, Ulenaers MJE, Spierings GACM, Cuppens R. Nanosecond switching of thin ferroelectric films. *Appl Phys Lett*. 1991;59(5):611-613.
105. Heyman PM, Heilmeier GH. A ferroelectric field effect device. *Proc IEEE*. 1966;54(6):842-848.
106. Shu-Yau W. A new ferroelectric memory device, metal-ferroelectric-semiconductor transistor. *IEEE Trans Electron Devices*. 1974;21(8):499-504.
107. Kwang-Ho K, Jin-Ping H, Soon-Won J, Tso-Ping M. Ferroelectric DRAM (FEDRAM) FET with metal/$SrBi_2Ta_2O_9$/SiN/Si gate structure. *IEEE Electron Device Lett*. 2002;23(2):82-84.
108. Miller SL, McWhorter PJ. Physics of the ferroelectric nonvolatile memory field effect transistor. *J Appl Phys*. 1992;72(12):5999-6010.
109. Ramesh R, Dutta B, Ravi TS, Lee J, Sands T, Keramidas VG. Scaling of ferroelectric properties in La-Sr-Co-O/Pb-La-Zr-Ti-O/La-Sr-Co-O capacitors. *Appl Phys Lett*. 1994;64(12):1588-1590.
110. Mathews S, Ramesh R, Venkatesan T, Benedetto J. Ferroelectric field effect transistor based on epitaxial perovskite heterostructures. *Science*. 1997;276(5310):238-240.
111. Chai X, Jiang J, Zhang Q, et al. Nonvolatile ferroelectric field-effect transistors. *Nat Commun*. 2020;11(1):2811.
112. Zheng Y, Ni G-X, Toh C-T, et al. Gate-controlled nonvolatile graphene-ferroelectric memory. *Appl Phys Lett*. 2009;94(16): 163505.
113. Naber RCG, Tanase C, Blom PWM, et al. High-performance solution-processed polymer ferroelectric field-effect transistors. *Nat Mater*. 2005;4(3):243-248.
114. Loke D, Lee TH, Wang WJ, et al. Breaking the speed limits of -phase-change memory. *Science*. 2012;336(6088):1566-1569.
115. Waser R, Aono M. Nanoionics-based resistive switching memories. *Nat Mater*. 2007;6(11):833-840.
116. Ho C-H, Lin C-H, Wang Y-P, Chen Y-C, Chen S-H, Huang Y-S. Surface oxide effect on optical sensing and photoelectric conversion of α-In_2Se_3 hexagonal microplates. *ACS Appl Mater Interfaces*. 2013;5(6):2269-2277.
117. Si M, Zhang Z, Chang S-C, et al. Asymmetric metal/α-In_2Se_3/Si crossbar ferroelectric semiconductor junction. *ACS Nano*. 2021;15(3):5689-5695.
118. Wang Z, Joshi S, Savel'ev SE, et al. Memristors with diffusive dynamics as synaptic emulators for neuromorphic computing. *Nat Mater*. 2017;16(1):101-108.
119. Xue F, He X, Wang Z, et al. Giant ferroelectric resistance switching controlled by a modulatory terminal for low-power neuromorphic in-memory computing. *Adv Mater*. 2021; 33(21):2008709.
120. Xia Q, Yang JJ. Memristive crossbar arrays for brain-inspired computing. *Nat Mater*. 2019;18(4):309-323.
121. Yang Y, Chen B, Lu WD. Memristive physically evolving networks enabling the emulation of heterosynaptic plasticity. *Adv Mater*. 2015;27(47):7720-7727.
122. Pfitzner A, Lutz HD. Redetermination of the crystal structure of γ-In_2Se_3 by twin crystal X-ray method. *J Solid State Chem*. 1996;124(2):305-308.
123. Groot CH, Moodera JS. Growth and characterization of a novel In_2Se_3 structure. *J Appl Phys*. 2001;89(8):4336-4340.

124. Jasinski J, Swider W, Washburn J, et al. Crystal structure of κ-In_2Se_3. *Appl Phys Lett*. 2002;81(23):4356-4358.
125. Almeida G, Dogan S, Bertoni G, et al. Colloidal monolayer β-In_2Se_3 nanosheets with high photoresponsivity. *J Am Chem Soc*. 2017;139(8):3005-3011.
126. Balakrishnan N, Steer ED, Smith EF, et al. Epitaxial growth of γ-InSe and α,β, and γ-In_2Se_3 on ε-GaSe. *2D Mater*. 2018;5(3):035026.
127. Yan W, Akimov AV, Page JA, et al. Nondestructive picosecond ultrasonic probing of intralayer and van der Waals interlayer bonding in α- and β-In_2Se_3. *Adv Funct Mater*. 2021;31(50):2106206.
128. Zhang X, Lee S, Bansal A, et al. Epitaxial growth of few-layer β-In_2Se_3 thin films by metalorganic chemical vapor deposition. *J Cryst Growth*. 2020;533:125471.
129. Xu C, Mao J, Guo X, et al. Two-dimensional ferroelasticity in van der Waals β′-In_2Se_3. *Nat Commun*. 2021;12(1):3665.
130. Hu Y, Feng W, Dai M, et al. Temperature-dependent growth of few layer β-InSe and α-In_2Se_3 single crystals for optoelectronic device. *Semicond Sci Technol*. 2018;33(12):125002.
131. Zhu M, Cojocaru-Mirédin O, Mio AM, et al. Unique bond breaking in crystalline phase change materials and the quest for metavalent bonding. *Adv Mater*. 2018;30(18):1706735.
132. Lee TH, Elliott SR. Chemical bonding in chalcogenides: the concept of multicenter hyperbonding. *Adv Mater*. 2020;32(28):2000340.
133. Shportko K, Kremers S, Woda M, Lencer D, Robertson J, Wuttig M. Resonant bonding in crystalline phase-change materials. *Nat Mater*. 2008;7(8):653-658.
134. Zhou J, Zeng Q, Lv D, et al. Controlled synthesis of high-quality monolayered α-In_2Se_3 via physical vapor deposition. *Nano Lett*. 2015;15(10):6400-6405.
135. Island JO, Blanter SI, Buscema M, van der Zant HSJ, Castellanos-Gomez A. Gate controlled photocurrent generation mechanisms in high-gain In_2Se_3 phototransistors. *Nano Lett*. 2015;15(12):7853-7858.

AUTHOR BIOGRAPHIES

Yu-Ting Huang received her BS (2017) degree from Jilin University, China. She is now a doctoral student at the State Key Laboratory of Integrated Optoelectronics, College of Electronic Science and Engineering, Jilin University. She mainly focuses on the structures, properties, and phase transitions of 2D ferroelectrics with first-principles calculations.

Nian-Ke Chen received his BS (2011), MS (2014), and PhD (2018) degrees from Jilin University, China. He is now an associate professor in the State Key Laboratory of Integrated Optoelectronics, College of Electronic Science and Engineering, Jilin University, and a core member of the Lab of Computational Semiconductor Physics, JLU (http://www.ioe-jlu.cn/csp/). His research interests are to reveal the underlying physics of microelectronic and optoelectronic materials and devices by first-principles calculations. He currently focuses on phase-change, ferroelectric, and resistive memory/computing technologies.

Xian-Bin Li received his BS (2005), MS (2007), and PhD (2010) degrees in microelectronics from Jilin University, China. He is currently a professor and the group leader of the Laboratory of Computational Semiconductor Physics in the State Key Laboratory of Integrated Optoelectronics, College of Electronic Science and Engineering, Jilin University (http://www.ioe-jlu.cn/csp/). He is also the head of the Department of Microelectronics Science and Engineering. He mainly focuses on the key problems in microelectronics and optoelectronics with the first-principles calculation, including phase-change memory physics, semiconductor defect physics, and light-matter interaction.

How to cite this article: Huang Y-T, Chen N-K, Li Z-Z, et al. Two-dimensional In_2Se_3: A rising advanced material for ferroelectric data storage. *InfoMat*. 2022;e12341. doi:10.1002/inf2.12341